Airborne measurements of surface albedo and leaf area index of snow-covered boreal forest

Terhikki Manninen[1], Jean-Louis Roujean[2], Olivier Hautecoeur[3†], Aku Riihelä[1], Panu Lahtinen[1], Emmihenna Jääskeläinen[1], Niilo Siljamo[1], Kati Anttila[1], Timo Sukuvaara[1] and Lauri Korhonen[4]

[1]Finnish Meteorological Institute, P.O. Box 503, FI-00101 Helsinki, Finland, terhikki.manninen@fmi.fi.

[2]CESBIO 18 avenue Edouard Belin, 31401 Toulouse, France

[3]Météo-France, Toulouse, France

[4]University of Eastern Finland, School of Forest Sciences, P.O. Box 111, 80101 Joensuu, Finland.

†Currently at: Exostaff GmbH/EUMETSAT, Darmstadt, Germany

Corresponding author: Terhikki Manninen (terhikki.manninen@fmi.fi)

Key Points:

- Surface albedo and effective leaf area index (LAI) can be measured at fine resolution and landscape scale simultaneously using helicopter
- Surface albedo and effective LAI are coherently retrieved based on a photon recollision probability based model
- Airborne and satellite-based surface albedo show a good agreement

Abstract

Helicopter based simultaneous measurements of broadband surface albedo and the effective leaf area index (LAI_{eff}) were carried out in subarctic area of Finnish Lapland in spring 2008, 2009 and 2010 under varying illumination and snow cover conditions. Vertical profile measurements show that the found relationship between albedo and LAI_{eff} seems to be rather independent of the flight altitude and therefore the footprint scale. Actually, flights above 500 m in altitude revealed low variations of the surface albedo approaching an aerial average at 1 km, meaning that a footprint of 20 km is representative of the landscape. The albedo was in the area beta distributed and without LAI_{eff} values below 0.25 the average albedo value of the area would decrease from 0.49 to 0.44 showing the albedo sensitivity to sparse vegetation. The results agreed with the photon recollision probability based model PARAS and the MODIS satellite albedo product MCD43A3. However, differences between satellite based and airborne albedo values were noticed, which could be explained by a difference in footprint size and/or the strong local heterogeneity as certain flights were operated on specific targets.

Plain Language Summary

Helicopter based measurements were used to assess how much a forest stand laying over a snow slab reduces the surface albedo at high latitudes where the sun zenith angle is large and shadow cast is always important. The effect is amplified in the case of sparse vegetation as there is less mutual shadowing. Model results and satellite observations are found in good agreement with the airborne data sets.

1 Introduction

Surface albedo is an Essential Climate Variable (ECV) as it determines the net radiation (GCOS, 2016). All changes in snow cover have a marked effect on the surface albedo, because fresh snow is a particularly highly reflecting target in the visible – with a slow decrease in the near infrared - compared to most land cover types with the exception of deserts. The boreal biome is characterized by tree stands laying above a snow layer about half a year today. Vegetation attributes strongly influence the snow-melting when the sun elevation is rapidly enhanced during springtime (Betts and Ball, 1997). Actually, leaf area index and snow form a complex system with close interactions (Verseghy et al., 1993; Manninen and Stenberg, 2009; Essery, 2013), Manninen and Jääskeläinen, 2018; Webster and Jonas, 2018; Jääskeläinen and Manninen, 2021). In the visible range, surface albedo is quite high – especially with fresh snow – and shadow cast by crown and trunk drives the landscape changes. In the infrared, radiation absorption by woody material initiates the processes of snow melt around trunks. Due to climate change, snow occurrence has reduced by several weeks in many areas in the boreal zone during the last decades (Brown and Mote, 2009; Derksen and Brown, 2012; Anttila et al, 2018; Bormann et al., 2018; Manninen et al., 2019).

Satellite based surface albedo products (Lucht et al, 2000; Schaaf et al., 2002; Govaerts et al., 2008; Anttila et al., 2016; Karlsson et al., 2017; Liu et al., 2013; Carrer et al., 2021) are able to provide global estimates of the surface albedo, but in regard to the sensitivity to several environmental factors – wind and air temperature may accelerate the processes – the collection of in situ measurements is mandatory to enhance our understanding and supports the validation exercise.. Continuous *in situ* measurements from ground-based networks offer the suitable temporal frequency to capture the dynamic of snow melt but they are not representative of the processes occurring at landscape scale. On the other hand, satellite-based surface albedo can offer a regional vision but with pixels of a moderate spatial resolution, thereby generating problems of representativity (Riihelä et al., 2010; Róman et al., 2010). It comes out that airborne albedo measurements meet the requirements in offering the appropriate flexibility in terms of time frequency, spatial resolution, and a large areal coverage.

Previously, airborne measurements have covered diverse sites: both ocean (Gatebe et al., 2005; Wendisch et al., 2004) and sea ice (Predoehl and Spano, 1965) and a wide variety of land cover types, both snow-covered (Ryan et al., 2017; Bergstrom et al., 2020) and snow-free (Gatebe et al., 2003; Webb et al., 2004; Wendisch et al., 2004; Cao et al., 2018). Seasonal variability of boreal forest albedo was investigated by Solantie (1988). The collected airborne albedo were used both for conducting modelling studies and for the validation of satellite-based albedo products.

Airborne measurements of broadband surface albedo covering large areas have mostly been carried out using airplanes with up- and down-facing pyranometers (Predoehl and Spano, 1965). The flight altitude has varied in the range 300 m (Solantie, 1988) - 2300 m (Predoehl and Spano, 1965). Spectral airborne albedo measurements have been carried out using airplanes with wavelength-scanning spectroradiometers (Webb et al., 2000; Webb et al., 2004; Gatebe et al., 2005). The altitude varied within 200 m (Gatebe et al., 2005), 600 m (Gatebe et al., 2003) and 370 m – 1700 m (Webb et al., 2004), 200 m – 500 m (Wendisch et al., 2004) and 800 m – 8 km (Román et al., 2011; Román et al., 2013).

Recently unmanned aerial vehicles (UAV) have become popular in measuring broadband surface albedo. First experiments were carried out using ordinary cameras (Ryan et al, 2017; Cao et al., 2018), but later on a quadcopter UAV has been used to carry the downward looking pyranometer, the upward looking pyranometer being at a fixed point in the flight area (Levy et al., 2018). As fixed wing UAVs are typically able to carry more weight than average quadcopters, they have also been used to carry both the up- and downward looking pyranometers (Ryan et al., 2017). The possibility to program the flight route of an UAV in advance enables carrying out very detailed flight plans. Fixed wing UAVs can in principle operate in a large area (range about 140 km) and the altitude may be as large as 600 m. On the contrary, the pilot of the quadcopter UAV has typically to keep eye contact to it and the maximum altitude is in practice about 100 m (Cao et al., 2018). However, aviation regulations may restrict the flight area and altitude allowed for the UAV. In addition, in winter conditions the practical limit for the flight lengths of quadcopters comes typically from the frequent need of battery recharging. The smaller UAVs can’t carry very heavy loads, which also limits the choice of the instrument to use. On the other hand, the quadcopters offer a very flexible possibility to study the reflectance characteristics of targets in three dimensions and will support modelling with data otherwise not achievable.

Helicopters have been used less frequently as a platform for airborne surface albedo measurements, probably because of problems related to irradiance measurements, as placing an upwards looking pyranometer unoccluded above the helicopter is not possible in practice. Hence, calibration of the global radiation measurements is challenging. Bergström et al. (2020) had one pyranometer below the helicopter registering the reflected radiation and the irradiance was observed at meteorological stations.

The advantages of a helicopter as the airborne platform are that 1) it is able to cover a large area over a short time, 2) the flight altitude is flexible enough to capture different footprint sizes, 3) vertical profiling is possible, 4) it can carry the expected payload to support the synergy of spectral data sets, 5) electricity is sufficiently available even in cold weather, 6) flight planning can be quickly adjusted to varying atmospheric conditions and 7) flight routes do not have to be linear as for an aircraft and it is possible to hover at a point and rotate 360° to sample BRDF (Bidirectional Reflectance Distribution Function).

This study presents surface albedo data measured during the SNORTEX (SNOw Reflectance Transition EXperiment) campaign from helicopter measurements acquired during 2008 – 2010 in Northern Finland (Manninen and Roujean, 2014, Manninen et al., 2012) using two pairs of pyranometers for observing both the irradiance and the reflected radiation. The test area belongs to northern boreal vegetation zone and subarctic climate zone. The data contains snow cover situations corresponding to pre-melt conditions and various phases of the melting season. The leaf area index (LAI) was measured simultaneously to radiation measurements from the helicopter (Manninen et al., 2009; Manninen et al., 2011). The goal of the whole study was to observe the variation of surface albedo of a forested area in diverse phases of the snow cover evolution. Of special interest was the relationship between the surface albedo and the effective leaf area index LAI_{eff}. Additional value comes from comparison with modelling and satellite products.

2 Data and Methods

2.1 Helicopter instrumentation

Two pyranometers on either side of the helicopter were used for the global radiation measurements and another two for reflected radiation measurements. The upwards and downwards looking sensors were attached back to back by the helicopter landing gear. Black plates between the pyranometers and the helicopter fuselage to prevent direct reflections from the fuselage (Figure 1). Super ellipsoid descriptions of the helicopter fuselage and rotors were used to analyze possible direct solar radiation reflections to the pyranometers. Mirror reflection from the helicopter fuselage to the pyranometers was not possible for the solar zenith angle values during the campaign. The pyranometers integrated and automatically stored the observed radiation within 10 s in 2008 and 2009. In 2010 the radiation value was integrated within 10 s and stored with an interval of 2 s. A time stamp and the latitude and longitude co-ordinates provided by GPS were attached to every measured quartet of radiance values and stored to the laptop, which also showed the measured values on the screen in real time. In 2009 also the altitude co-ordinate provided by GPS was integrated in the system.

For airborne LAI measurements a Canon pocket camera A640 with a 0.7 × wide angle conversion lens WC-D58N was attached to the helicopter landing gear so that it was looking orthogonally downwards. The angle from the image center was about 41° at the corners of the rectangular images and 35° and 28° at the middle of the image edges (Manninen et al., 2009; Manninen et al., 2011). The images were taken by the Karhukamera system every three seconds and the 3-D GPS coordinates with time stamps were registered for each image frame. The images were stored in standard jpg format directly to a laptop used for operating the camera. During the flight the latest image was repeatedly sent to the screen of the laptop to enable choice of optimal route and altitude. Hence, two independent GPS-coordinate sets (pyranometer and camera systems) were available for the flights to guarantee accurate temporal combination of the pyranometer and LAI data sets. A pressure gauge and a thermometer were integrated in 2009 and 2010 to the pyranometer system to achieve better altitude accuracy at low altitudes.

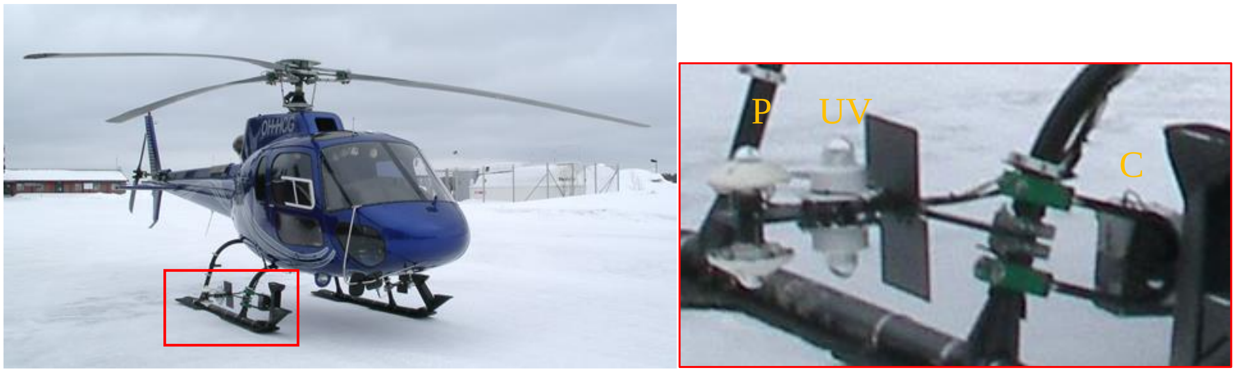

Figure 1. Pyranometer (P), UV sensor (UV) and camera (C) attachment to the helicopter. The other pairs of pyranometers and UV sensors are attached to the opposite landing gear symmetrically. The thermometer and the humidity sensor at attached at the back of the opposite landing gear below the fuselage.

In addition there were two pairs of UV sensors and a Pt100 thermometer and a humidity sensor (humicap) attached to the helicopter, the UV sensors being between the pyranometers and the black plates (Figure 1). In all flights except the cloudy days, March 13, 2009 and April 24, 2009, there was also the shortwave multi-directional instrument OSIRIS (airPOLDER) beneath the back part of the fuselage (Manninen et al., 2012). See section 2.2 for a full listing of measurement flights undertaken with the helicopter.

2.2 Flights during the SNORTEX campaign

The studied area represents subarctic boreal forest (Figure 2) and the flights were carried out within an area with corner co-ordinates (67.258°N, 26.2253°E) and (67.9263°N, 27.3897°E), all co-ordinates are in WGS84 system. In order to capture the albedo variation from pre-melt conditions to melting snow conditions and after melt snow-free conditions, the flights in 2009 were carried out in March, April, and May. Both cloudy and cloud-free conditions (Figure 3, Figure S1 in Supplementary material) were available before and after the snow melt started. Some of the horizontal flight routes were planned so that the helicopter was measuring in four wind directions above a site of interest (mainly for the OSIRIS instrument), some routes provided a grid over the intensive test area of ground measurements of 2009 and 2010 (Manninen and Roujean, 2014). Some longer transects were also flown. Since winters are not all similar, flights were carried out in three years (2008, 2009 and 2010) to cover the natural variation of the snow-covered area albedo.

Figure 2. Example photos of the study area showing varying forest density in April 24, 2009. The flight altitude was about 880 m.

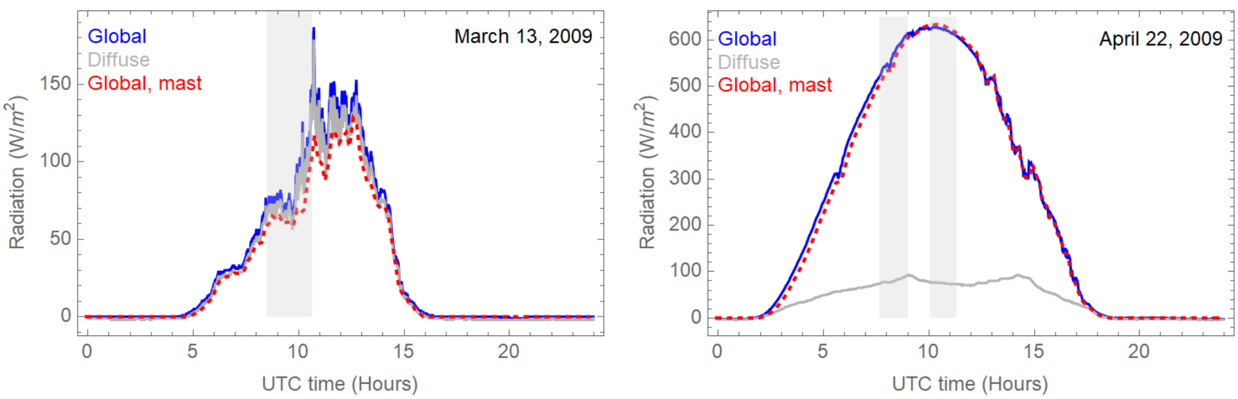

Figure 3. The global and diffuse radiation observed at the sounding station (solid curves) and the global radiation observed at the Sodankylä Heikinheimo mast (dashed curves) on the flight days March 13, 2009 and April 22, 2009. The times of the flights are shown in light gray bars.

The vertical flights were planned partly to test the airborne LAI retrieval quality and partly to study, how the altitude variation impacts the albedo variation, i.e. how the albedo varies with spatial resolution. Namely, when using pointwise *in situ* albedo measurements, the areal representativity of the ground based measurements is always an issue.

Table 1. The pyranometer flights carried out in the SNORTEX campaign in 2008 – 2009.

Date	Flight time [UTC hour]	Sky conditions during the flights	Flight altitude above ground [m]	Flight pattern	Comments
April 2, 2008	10.7 — 12.0	Clear/cloudy	20 — 280	Vertical profiles	
April 3, 2008	10.3 — 12.4	Clear	830	Horizontal line and wind rose	
April 7, 2008	13.7 — 14.9	Clear	50 — 800	Horizontal line and crosses	
April110, 2008	13.2 — 14.7	Clear	~ 120	Horizontal line and crosses	No LAI or altitude data
March 13, 2009	8.5 — 10.6	Cloudy	20 — 320	Vertical profiles	
March 17, 2009	11.1 — 14.2	Clear	280	Crosses over test sites	
March 18, 2009	8.9 — 9.0	Clear/cloudy	50 — 450	Crosses over test sites	No LAI_{eff} data
April 22, 2009	7.7 — 9.0	Clear	280	Crosses over test sites	
	10.0 — 11.3	Clear	880	Grid over test area	Camera co-ordinates partly missing
April 24, 2009	7.5 — 8.8	Clear / cloudy	250, 120	Crosses over test sites	Missing camera co-ordinates
	10.4 — 10.7	Cloudy / clear	880	Grid over test area	
	11.2 — 11.9	Cloudy / clear	880	Grid over test area	
May 4, 2009	13.2 — 14.3	Clear -> cloudy	200	Crosses over test sites	
May 5, 2009	6.3 — 8.0	Cloudy -> clear	170	Long transect	Partly large difference in illumination conditions at the sounding station
March 18, 2010	11.4 — 12.2	Clear/cloudy	600	Horizontal North-South flight lines over lake and aapa mire	Co-ordinate matching of camera and pyranometer not possible due to GPS failure.
March 19, 2010	11.3 — 15.0	Clear/cloudy	20 — 300	Vertical profiles	

On some days more than one flight was planned, but occasionally a flight had to be interrupted because the helicopter was needed to rescue service. Sometimes also the flight was interrupted due to instrument failure. The flight route patterns are shown in Appendix A. The flights carried out in May 4 and May 5, 2009 were dedicated to partial snow measurements, since most of the snow cover had already melted during that area.

2.3 Airborne albedo data and its calibration

As the helicopter is far from being an ideal platform, besides the normal radiometric instrument calibration the measurement configuration has to be calibrated as well. All four pyranometers were radiometrically calibrated before the campaigns using the standard procedure of Finnish Meteorological Institute (FMI).

The configuration calibration contains the following steps: 1) azimuthal calibration, 2) first albedo magnitude calibration and 3) flight altitude correction, 4) final albedo magnitude calibration. The azimuth effect has to be checked, because the illumination conditions of the upwards looking pyranometers are different, when the helicopter is flying towards the sun (or the opposite direction) or perpendicularly to the principal plane (the plane where the target and the Sun are aligned). The effect of the atmospheric attenuation on the global and reflected radiation depends on the flight altitude and must be corrected for. That process requires knowledge about the surface albedo. Hence, we derive first an estimate of the surface albedo assuming no atmospheric effect (Section 2.3.2) and use it as input for the atmospheric correction of the global and reflected radiation (Section 2.3.3). After that correction the final surface albedo estimate is calculated anew using the atmospherically corrected global and reflected radiation values (Section 2.3.4).

2.3.1 Azimuthal calibration

The azimuthal dependence of the global and reflected radiation was measured in cloudy and clear-sky conditions above forest at the immediate vicinity (67.3625°N, 26.6415°E) of the Sodankylä Heikinheimo mast (67.361866°N, 26.637728°E) of the Arctic Space Centre of Finnish Meteorological Institute, where the surface albedo is operationally measured at 45 m height at 10 min interval. The helicopter hovered at that height in eight azimuth directions starting from direct view to the sun. The whole circle took about 5 minutes. This data was used to check the azimuth dependence of the measured radiation data. In addition, it was used to derive the shading correction coefficient for the reflected radiation.

First the time dependence coefficient k_g of the global radiation I_g measured at the mast was determined

$$k_g = \frac{(I_g - I_{g0})}{<I_g>} \quad , \tag{1}$$

where I_{g0} refers to the value of I_g at the beginning of the time window and <> denotes the average. Since the time window was so short, it was sufficient to use linear approximation of the time dependence of I_g. Either the variation was extremely small ($k_g < 0.4\%$) or the R^2 value for the linear relationship of I_g was high, the variation range being 0.984 — 0.99997. Then the variation of the airborne global radiation values of the left and right pyranometers (I_{gleft} and I_{gright}) multiplied by (1-k_g) was analyzed vs. the azimuth angle of the helicopter direction. A clear sinusoidal dependence was observed for both pyranometers (Table 2) both in clear-sky and cloudy conditions, but understandably the variation range was markedly larger in clear-sky conditions due to shadowing of the fuselage. The right and left pyranometer global radiation had a phase difference of 180°, as expected, so that all the time either of the two upwards looking pyranometers avoided shading of the fuselage. The variation of the reflected radiation did not show as systematic time dependence (as it was really small), hence no temporal correction was made to it in the azimuthal analysis.

The following combination of I_{gleft} and I_{gright} was rather insensitive to the azimuth angle and was used as the basis of deriving the calibrated airborne global irradiance

$$I_{gc} = < \max(I_{gleft}, I_{gright}) + \frac{(I_{gleft}+I_{gright})}{2} > \quad . \tag{2}$$

Essentially I_{gc} represents an estimate of the sum of the direct radiation and the diffuse radiation, but it must still be calibrated, as some of the diffuse radiation is occluded. For the completely cloudy day of March 13, 2009 the global radiation observed by the left and right pyranometers was practically identical (Figure 4), since the amount of direct radiation was then negligible.

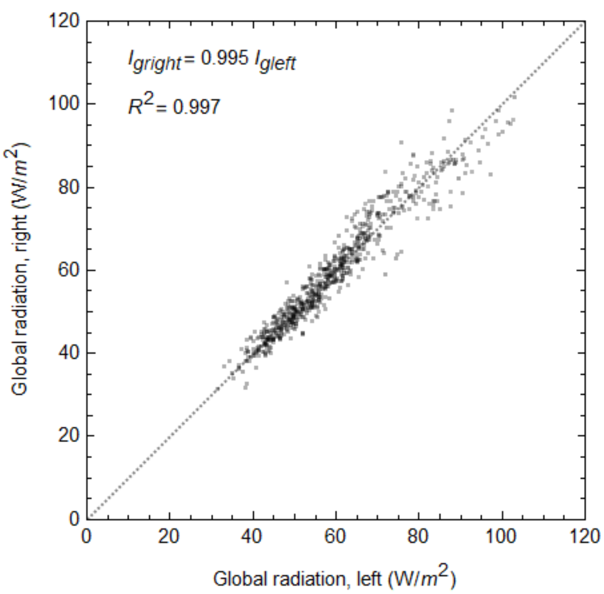

Figure 4. The global radiation measured by the right pyranometer vs. that of the left pyranometer for the flight carried out in March 13, 2009 (Table 1) before calibration and removal of tilted data.

The reflected radiation observed by the left and right pyranometer was very similar for all flights, except when the helicopter was markedly tilting at turning points. Hence, there is no need to calibrate the right and left downwards looking pyranometers separately, and the reflected radiation I_r to be calibrated was chosen to be

$$I_{rc} = \frac{(I_{rleft}+I_{rright})}{2}. \tag{3}$$

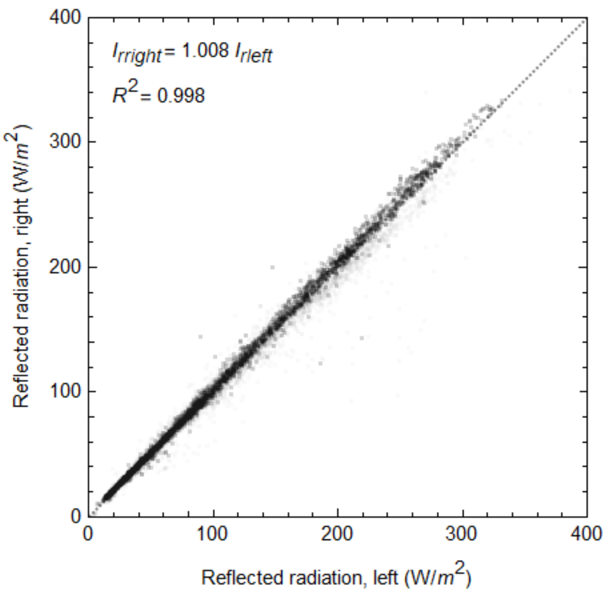

Figure 5. The reflected radiation measured by the right pyranometer vs. that of the left pyranometer for all data from all flights (Table 1) before calibration and removal of tilted data.

The variation of the airborne global and reflected radiation of the left and right pyranometers with the azimuth direction is characterized in (Table 2).

The uncalibrated albedo α_{gc} was now derived to be

$$\alpha_{gc} = \frac{I_{rc}}{I_{gc}} \quad . \qquad (4)$$

The variation of α_{gc} as a function of the azimuth angle was very small for clear and cloudy conditions, but understandably slightly larger for the mixed case of March 19, 2010 (Table 2) due to varying cloudiness during the azimuthal circle. In addition, some of the variation of the albedo was due to the uneven helicopter motion between stabilized azimuth direction positions. Since the azimuth dependence is related to the measurement geometry, it is reasonable to assume that the azimuth effect on the albedo is of the same order for all flights in the same conditions.

In perfectly clear-sky conditions when the helicopter is perpendicularly to the sun the airborne pyranometer of the sunny side measures the direct radiation and a fraction of diffuse radiation, while the pyranometer on the opposite side of the helicopter measures just the same fraction of the diffuse irradiance. Comparing the ratio *r'* of the shaded and sunny side pyranometer irradiances, I_{shade} and I_{sunny} respectively, to the ratio of the diffuse irradiance to the global irradiance measured at the sounding station, *r*, one can derive the correct global radiation for the airborne measurements I_a to be

$$I_a = \frac{(1-r')}{(1-r)} I_{sunny} \qquad (5)$$

Table 2. Azimuth dependence of the airborne radiation measured at the Sodankylä Heikinheimo mast. The 80% variation range normalized with the mean value and the coefficient of determination for the sinusoidal dependence of the global radiation on the azimuth angle for the left and right airborne pyranometers. The ratio of the standard deviation and the mean of the averaged airborne global and reflected radiation and mean and standard deviation of albedo, $\sigma_{gc}/<I_{gc}>$, $\sigma_{rc}/<I_{rc}>$, $<\alpha_{gc}>$ and $\sigma_{\alpha gc}$ respectively, measured at 45 m level beside the Sodankylä Heikinheimo mast at the Arctic Space Centre of Finnish Meteorological Institute, where the surface albedo is operationally measured above a forest. The azimuth directions of the helicopter were 0°, 45°, 90°, 135°, 180°, 225°, 270°, 315° and 360° between the sun and the helicopter fuselage.

Date	Sky	Solar zenith angle	$\frac{I_{diffs}}{I_{gs}}$	Sinusoidal characteristics				$\frac{\sigma_{gc}}{<I_{gc}>}$ [%]	$\frac{\sigma_{rc}}{<I_{rc}>}$ [%]	Albedo	
				$I_{gleft}(1-k_g)$		$I_{gright}(1-k_g)$				$<\alpha_{gc}>$	$\sigma_{\alpha gc}$
				80% range/ mean	R^2	80% range/ mean	R^2				
April 2, 2008	Clear	63.4°	0.31	122	0.971	115	0.980	11.7	9.4	0.185	0.009
March 13, 2009	Cloudy	70.1°	0.94	18	0.999	5.1	0.998	3.8	5.3	0.224	0.007
April 22, 2009	Perfectly clear	60.1°	0.14	143	0.926	158	0.827	7.3	1.9	0.166	0.015
April 24, 2009	Cloudy/ clear	60.1°	0.73	71	0.975	62	0.936	7.8	11.1	0.183	0.010
March 19, 2010	Clear/ cloudy	80.3°	0.50	92	0.979	127	0.978	13.7	9.7	0.166	0.030

For April 22 the calibration factor (1-r')/(1-r) was 1.037. The empirical ratio $<I_g>/<I_{gc}>$ was 1.039 for the same calibration time window. So, a good accuracy can be obtained carrying out an empirical calibration of the global radiation using I_{gc}. This was the approach taken (presented in the following Section), because measurements were carried out also in other direction vs. the sun than perpendicular. Since I_{gc} was relatively independent of the azimuth direction, the calibration should be reliable in all directions. It is noticeable that the airborne global irradiance was underestimated only by 4%, but the reason is that the sky was perfectly clear at that time and the solar zenith angle was not larger than 60.1°. In more cloudy sky and/or larger solar zenith angle the fraction of diffuse irradiance would be larger and consequently also the underestimation of the global irradiance would be larger. Therefore, it is essential to calibrate the airborne global irradiance using simultaneously measured empirical values.

2.3.2 First radiation magnitude calibration

The next step of the calibration was to correct the magnitudes of the global and reflected radiation. This is carried out by comparing the airborne measurements to global (I_g) and reflected (I_r) radiation measurements operationally carried out at the mast with 10 min interval and to global irradiance (I_{gs}) measurements operationally carried out with 1 minute interval at the

Tähtelä sounding station (67.36664°N, 26.628253° E). In the clearest sky conditions the agreement between the global radiation values at the mast and at the sounding station were very similar (Table 3) in spite of the 667 m distance between the mast and the sounding station. Also, the airborne global irradiance I_{gc} had a good correlation with them. When the flight altitude varied markedly, the R^2 values between I_{gc} and I_{gs} were taken separately for two or three patches and their mean value is shown in the table. Besides the weather conditions, also the distance between the helicopter and the sounding station and possible tilting of the helicopter (at turning points) could reduce the R^2 value. The correlation between I_{gleft} and I_{gright} was high (Appendix B, Table B1), when the sky was cloudy, because then there was mainly diffuse radiation. At clear sky conditions their correlation could be high only, if the helicopter was flying towards the sun (or vice versa).

Table 3. The relationship between the global irradiance measured at the Sodankylä Heikinheimo mast (I_g) and at the sounding station (I_{gs}) for the flight times. The R^2 values for the linear relationship between the airborne irradiance I_{gc} and I_{gs} are given as well. Notice that the R^2 values were derived for a linear regression without allowing a constant.

Date	I_g vs. I_{gs}		I_{gc} vs. I_{gs}
	$\frac{\lvert < I_g > - < I_{gs} > \rvert}{< I_{gs} >}$ [%]	R^2	R^2
April 2, 2008	4.0	0.967	0.887
April 3, 2008	2.9	0.9998	0.968
April 7, 2008	2.7	0.9997	0.961
April110, 2008	0.4	0.983	0.927
March 13, 2009	5.6	0.989	0.963
March 17, 2009	3.7	0.9997	0.872
March 18, 2009	0.2	0.999	0.964
April 22, 2009	0.5	0.9999	0.993
April 24, 2009	3.3	0.980	0.957
May 4, 2009	4.9	0.972	0.896
May 5, 2009	11.2	0.932	0.929
March 18, 2010	2.5	0.995	0.933
March 19, 2010	4.3	0.985	0.946

The reflected radiation measured by the left and right pyranometers was practically identical unless the helicopter was tilted sideways. The fuselage of the helicopter did not shade the downwards looking pyranometers, but the skids of the helicopter and the black plates between the sensors and the fuselage occluded their view to some extent. As the configuration was the same for all flights, it was sufficient to determine the calibration coefficient c_r of the reflected radiation only once using the data of the best day, April 22, which was perfectly clear at the time window of the calibration. So, c_r was calculated from

$$c_r = \frac{<I_r>}{\langle (I_{rleft} + I_{rright})/2 \rangle} \tag{6}$$

where $< I_r >$ was the temporal mean of the reflected radiation observed at the mast during the time (UTC 7:42:15 – 7:47:35) the helicopter was hovering in its vicinity at the same altitude and $<(I_{rleft} + I_{rleft})/2>$ was the mean of the reflected radiation of the left and right downwards looking pyranometers of the helicopter, recorded at the same time window as $<I_r>$. As the altitude of the pyranometers at the mast is 45 m above ground, they get 90% of the reflected radiation from an area having a radius of 450 m. Hence, in direct illumination conditions it does not matter much that the helicopter was hovering at a point about 140 m from the mast. However, for diffuse radiation (March 13, 2009) the reflected radiation observed at the mast was dominated by the snow-covered clearing right beneath the mast, hence causing somewhat larger albedo value than would be that of the forest. The global radiation I_{gc} was calibrated vs. the global radiation measured at the sounding station with an interval of 1 min, because at the mast it was recorded only as 10 min averages. The correction factor c_m was defined as the ratio of the median values of I_{gc} and I_{gs}

$$c_m = \frac{\widetilde{I_{gs}}}{\widetilde{I_{gc}}} \tag{7}$$

where ~ denotes the median. The first estimate for the true airborne global radiation I_{ga} is then

$$\hat{I}_{ga} = c_m I_{gc} \tag{8}$$

where ^ denotes an estimated value. Some flights had two or three distinct relatively constant flight altitudes. Then the value for c_m was derived separately for the patches of constant altitude. The c_m value of the lowest altitude was used for the rest of the data.

So far, the calibration of the airborne global radiation could be of high quality only, if the flight altitude were so small that atmospheric effect on it does not have to be taken into account. However, taking the atmosphere into account requires some knowledge of the surface albedo. Hence, we used the calibration derived so far to retrieve as input for the atmospheric calibration the temporary surface albedo estimates that are derived as follows

$$\hat{\alpha}_a = \frac{c_r(I_{rleft}+I_{rright})/2}{c_m I_{gc}} \quad . \tag{9}$$

2.3.3 Flight altitude correction

The next step of the calibration was to take into account the effect of the flight altitude (Boers et al., 1998). The diffuse and global irradiance measured at the sounding station were used to retrieve the direct (but attenuated) solar radiation S, which is the difference of the global and diffuse irradiance. Then the optical thickness τ of the atmosphere (at the surface) was derived from the equation (Sekera and Kahle, 1966; Kahle, 1968)

$$S = \pi F_0 \mu_0 e^{-\tau/\mu_0} \quad , \tag{10}$$

where πF_0 is the incident flux and μ_0 is the cosine of the solar zenith angle θ_0. The variation of the airborne global and reflected radiation with flight altitude were taken into account by assuming that the optical thickness is linearly related to the flight altitude and the height of the tropopause was taken to be 8.5 km (which is a realistic value for the polar areas in winter (Geerts and Linacre, 1997). The linearity assumption is reasonable, as the flight altitude was relatively low (50 m … 1 km). The global and reflected radiation values were transformed from the flight altitude values to surface values by the relationship of the upward H_d and downward G_d radiation dependence on the altitude and optical thickness of the atmosphere (Kahle, 1968)

$$G_d = \pi F_0 \mu_0 \left[\frac{\gamma_l(\mu_0)+\gamma_r(\mu_0)}{2(1-A\bar{s})}\right] \tag{11}$$

$$H_u = \pi F_0 \mu_0 \left[1-(1-A)\frac{\gamma_l(\mu_0)+\gamma_r(\mu_0)}{2(1-A\bar{s})}\right] \tag{12}$$

where A is the ground reflectivity and the functions γ_l, γ_r and $\bar{s}$ are defined by Chandrasekhar (Kahle, 1968). They are calculated using the table compiled by Natraj and Hovenier (2012). The correction factors for c_a related to removal of the effect of the flight altitude is obtained from

$$c_a = \frac{\frac{\gamma_{la}(\mu_0)+\gamma_{ra}(\mu_0)}{2(1-A\bar{s}_a)}}{\frac{\gamma_l(\mu_0)+\gamma_r(\mu_0)}{2(1-A\bar{s})}} \tag{13}$$

where the values for γ_l, γ_r and $\bar{s}$ are calculated at the surface and for γ_{la}, γ_{ra} and $\bar{s}_a$ at the flight altitude, which was available for each point from the pressure gauge. Here we used $A = \hat{\alpha}_a$. The airborne global I_{ga} and reflected I_{ra} radiation corrected for the altitude are now

$$I_{ga} = c_a I_{gc} \tag{14}$$

$$I_{ra} = \left(I_{rleft} + I_{rright}\right)/2 + (1 - c_a)I_{gc} \tag{15}$$

Since $c_a \leq 1$, the reflected radiation is larger, the global radiation smaller and the surface albedo larger than the ones measured at higher altitudes. However, at this stage the measured radiation components are corrected only for the altitude and the configuration of the shading effect correction presented in the previous section must still be carried out.

2.3.4 Final radiation magnitude calibration

The global radiation was now corrected for the configuration effects by requiring the median of the airborne altitude corrected global radiation to match the median of simultaneous global radiation measurements at the sounding station like in Eq. 7 so that the completely calibrated airborne global radiation I_{gt} is

$$c_t = \frac{\widetilde{I_{gs}}}{\widetilde{I_{ga}}} \quad . \tag{16}$$

$$I_{gt} = c_t I_{ga} \quad . \tag{17}$$

The completely calibrated airborne reflected radiation I_{rt} is obtained from

$$I_{rt} = c_r I_{ra} \tag{18}$$

using the value c_r = 1.1697 derived for the clearest day, April 22, for all flights, because it is only due to the geometry of the measurement configuration. The airborne calibrated albedo α is finally

$$\alpha = \frac{I_{rt}}{I_{gt}} \tag{19}$$

Values for the calibration parameters c_m and $<c_a>$ and c_t are given in Table 4 for all flights. In addition, the ratio of the mean calibrated albedo and the mean uncalibrated albedo are shown for each flight. Mostly the calibration coefficients are essentially of the same order in similar sky conditions. However, in May 5, 2009 the first patch had a distinctly different calibration coefficient c_m due to varying cloudiness. The timing of the cloud disappearance differed at the helicopter and the mast, which showed then in more distinct discrepancy of the airborne and sounding station global radiation level. For the same reason on that day also the global radiation measured at the mast deviated markedly from that of the sounding station (Table 3). Hence, the first part of the data of May 5, 2009 was discarded, because the calibration of the global radiation would not have been reliable.

Table 4. Calibration coefficients for the global radiation derived for various flights. When there were several constant altitudes, the coefficient c_m was derived separately for each of them.

Date	Sky conditions during the azimuthal calibration	c_m	$<c_a>$	c_t	$\frac{<\alpha>}{<\alpha_{gc}>}$
April 2, 2008	Clear (mostly)	1.15	0.993	1.16	1.04
April 3, 2008	Clear	1.09	0.974	1.12	1.13
April 7, 2008	Clear	1.20, 1.11	0.989	1.13	1.06
April110, 2008	Clear	1.12	0.996	1.13	1.04
March 13, 2009	Cloudy	1.31	0.992	1.32	0.90
March 17, 2009	Perfectly clear	1.05	0.991	1.07	1.12
March 18, 2009	Clear/cloudy	1.11	0.993	1.12	1.06
April 22, 2009	Perfectly clear	1.09, 1.08	0.982	1.12	1.11
April 24, 2009	Clear -> cloudy	1.10, 1.35, 1.36	0.961	1.39	0.98
May 4, 2009	Clear -> cloudy	0.91	0.988	1.12	1.15
May 5, 2009	Cloudy -> clear	(2.02,) 0.96	0.992	(2.04,) 0.97	0.77
March 18, 2010	Clear/cloudy	0.92	0.989	0.93	0.86
March 19, 2010	Clear/cloudy	1.01	0.998	1.07	1.10

Table 5. The relationship between the airborne calibrated albedo and that measured at the Sodankylä Heikinheimo mast. The LAI_{eff} value previously measured at ground closest to the mast was 0.41 (Manninen and Riihelä, 2009) and the airborne LAI_{eff} varied slightly at the calibration points.

Date	Latitude	Longitude	Sky	$\frac{I_{diffs}}{I_{gs}}$	Solar zenith angle	Albedo at mast		Airborne albedo		Airborne LAI_{eff}	
						Mean	Median	Mean	Median	Mean	Standard deviation
April 2, 2008	67.3617°	26.6367°	Clear	0.31	63.2°	0.185	0.184	0.206	0.204	1.17	0.11
March 13, 2009	67.3624°	26.6413°	Perfectly Cloudy	0.94	70.1°	0.261	0.263	0.198	0.199	1.18	0.06
April 22, 2009	67.3622°	26.6409°	Perfectly clear	0.14	60.1°	0.184	0.184	0.179	0.174	1.32	0.11
April 24, 2009	-	-	Cloudy	0.73	60.1°	0.182	0.183	0.195	0.167	1.11	0.05
March 19, 2010	67.3621°	26.6401°	Clear /cloudy	0.50	80.0°	0.211	0.211	0.221	0.224	0.72	0.09

2.4 Airborne LAI data

The wide-optics camera data was used for LAI estimation essentially similarly as fish-eye photos, the white snow serving as the background. The airborne LAI estimates were validated with ground based measurements (Manninen et al., 2009; Manninen et al., 2012). The images were thresholded automatically (Nobis and Hunziker 2005; Ridler and Calvard 1978) to separate forest canopy pixels from the background snow. The resultant binary images were used to compute canopy gap fractions for off-nadir angle ranges 0–10°, .., 10–40°. The gap fractions were used to compute LAI_{eff} for each image using the well-known formula proposed by Miller (1967). The results were compared with hemispherical fisheye images obtained *in situ* that were analyzed in a similar manner. A simple linear regression fit between the estimates (LAI_{ground} = 1.03 LAI_{eff} - 0.04) had an R^2 of 0.96 (Manninen et al. 2012).

2.5 Operational radiation measurements

The global and diffuse radiation is operationally measured at Sodankylä at the FMI sounding station (67.36664°N, 26.628253°E) with a one minute interval using a Kipp & Zonen CM11 Pyranometer and a tracker. In addition, the global and reflected radiation is measured with a 10 minute interval at the Sodankylä Heikinheimo mast (67.361866°N, 26.637728°E) in a Scots pine dominated mature forest at an altitude of 45 m above the ground and well above the tree tops using a Kipp & Zonen CM11 Pyranometer.

2.6 Satellite data

The satellite based albedo values used in this study are the MODIS based MCD43A3 white sky and black sky albedo products (Schaaf et al. 2002). They are daily products that are based on 16 days of local solar noon data, temporally weighted to the ninth day. The data is in 500m resolution. The products include quality flags. Only data with the highest quality classification was used in this study. For March 13th and April 24th (cloudy days) the analysis is based on the WSA_shortwave product (white sky albedo), and for the rest of the days the

BSA_shortwave (black-sky-albedo) data was used. However, for the solar zenith angles of the campaign the black-sky and white-sky albedo values are very similar.

2.7 Albedo modelling

Albedo modeling is performed using the vegetation dependent PARAS albedo model (Rautiainen and Stenberg, 2005; Smolander and Stenberg, 2005; Stenberg et al., 2016). The basis of the PARAS model albedo calculation is the photon recollision probability p. That is a probability of an event in which a photon, after being scattered from a leaf in a canopy, interacts with that same canopy again. When p and leaf single scattering albedo (ω_L) are known, the total amount of radiation scattered by the canopy is possible to estimate at any wavelength. The PARAS albedo model was extended by Manninen and Stenberg (2009) by adding multiple scattering between canopy and ground to include effect of highly reflective background (i.e. snow). Extended PARAS model has been used to model boreal forest albedo (Manninen and Stenberg, 2009; Manninen and Jääskeläinen, 2018; Jääskeläinen and Manninen, 2021). Detailed model formulas are presented in Appendix C.

The model was first compared with the vertical profile data of March 13, 2009, which was a completely cloudy day. The model was used to simulate the albedo in visible and near infrared bands. The broadband albedo was derived using the conversion formula by Liang (2000). The broadband albedo of the forest floor was taken to be the mean of the values for which LAI_{eff} was 0, excluding one aapa mire related darker value. The corresponding spectral albedo of visible and near infrared bands were obtained on the basis of the reflectance ratio of those bands of the snow spectra measured in March 13, 2009 (Manninen et al., 2021). The leaf single scattering albedo for the visible and near infrared bands, $\omega_{red} = 0.068$ and $\omega_{nir} = 0.697$, were taken to be 15% smaller than the smallest values measured by Hovi et al. (2017) for the season May – October to take into account the seasonal difference. As the modelling result looked convincing, those single scattering albedo values were used for all modelling calculations.

The forest floor albedo for other days were derived similarly as for March 13, 2009. The spectral albedo ratio of March 13 was used for all pre-melt snow conditions (2008, March 2009 and 2010). For April 2009 the measured spectra of April 22, 2009 (Manninen et al., 2021) were used for deriving the forest floor spectral albedos from broadband albedo.

The model was used for normalizing the albedo values to match the solar zenith angle of 60° in order to make the albedo values of diverse days directly comparable and to be able to derive the total albedo distribution for analyzing the effect of LAI_{eff} on it. It should be noted that this could be done only for days, for which airborne LAI_{eff} data was available.

2.8 Analysis of airborne data

The pyranometer and camera measurements were co-registered with their independent time codes checking the match by comparison of their independent co-ordinate information. In 2008 only the camera GPS provided the altitude, which was then used for the vertical profiles, interpolating missing values linearly. In 2009 and 2010 the pressure gauge of the pyranometer system provided gap free vertical co-ordinates, which were used for the vertical profiles. The flight altitude was compared to the above sea level height of the helicopter station, which was 185 m. However, there are some hills in the flight area, so that the flight altitude is not exactly everywhere the same amount above the ground. The vertical profiles were equally high every place and started from close to the tree top level (Figure S2 in Supplementary material). For vertical profiles 10% difference was allowed for the left and right reflected radiation value to have more data per profile. For other flights only a 5% difference was allowed.

The relationship between LAI_{eff} and albedo was first analyzed for each vertical profile of three individual days (April 2, 2008, March 13, 2009, and March 19, 2010). The results were compared to the PARAS modelling (Section 2.7) results. Then the PARAS model was used to normalize the albedo data to correspond to the solar zenith angle of 60° in order to be able to compare the diverse flight data with each other and to derive the albedo distribution for the region. This could be carried out only for data for which simultaneous LAI_{eff} values were available.

Finally, the airborne data was then co-registered with MODIS data by grouping the airborne parameter values according to which pixel their horizontal co-ordinates were located. For cloudy days (March 13, 2009 and April 24, 2009) airborne data was compared to the white-sky shortwave albedo product of MODIS, for the rest the black-sky shortwave albedo product was used. As the MODIS product is normalized to local midday, the airborne data had to be normalized to that. Since the scenery was very heterogeneous, it was not possible to use the PARAS model or a normalization scheme derived for a certain target (Yang et al., 2008; Manninen et al., 2020). Using the whole data mass per day a statistical relationship was derived by linear regression between the solar zenith angle and the albedo. Both the hyperbolic cosine of the normalized azimuth (Manninen et al., 2020) and the cosine of the solar zenith angle using the functional form by Yang et al. (2008) were tested as predictors and the correction was the same for both alternatives. This relationship was then used to normalize the airborne albedo values to local noon. The comparison between the airborne and MODIS data was carried out using the airborne data normalized this way.

3 Results

3.1 Variation of albedo with LAI

The simultaneously measured airborne albedo and LAI_{eff} values of the three days of vertical profiles (April 2, 2008, March 13, 2009 and March 19, 2010) were compared to each other and modelling results (Figure 6). The individual outliers correspond to cases, where the area seen by the camera differs markedly from its near surroundings, which affect the albedo value. Since March 13, 2009 was a completely cloudy day, there is no need to pay attention to the solar zenith angle varying from profile to another. Contrarily, in April 2, 2008 and March 19, 2010, the day was clear, and the solar zenith angle varied in the range 62.6° — 64.5° and 75.6° — 82.6°, respectively. Because the sun elevation was so low, the albedo of the point in question could not be accurately normalized to a fixed solar zenith angle value using only information related to point itself, because the albedo would depend also on possible shading form the nearby region. Hence, the data shown in Figure 7 and Figure 8 are not normalized and for 2008 and 2010 some of the scatter of the points comes from varying solar zenith angle and shadows. Also, the varying fraction of diffuse irradiance caused some scatter with respect to the mean modelled curve. The outliers of the clear day of 2010 are clearly caused by heterogeneous surroundings. In Figure 9 left the LAI_{eff} is measured at a lower altitude from the forest at the image center, but the open area in its immediate vicinity increases the albedo value. In Figure 9 right the opposite effect takes place, the surrounding forest decreases the albedo, but LAI_{eff} measured at a lower altitude has the value of the open area in the center.

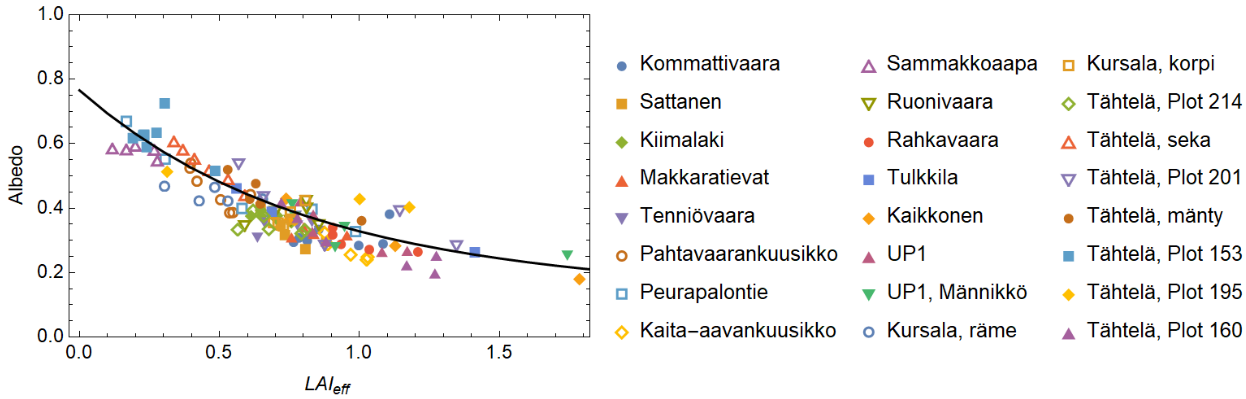

Figure 6. Variation of the airborne albedo with the airborne LAI_{eff} of the vertical profiles measured in March 13, 2009. The profile height was about 200 m. The black curve shows the PARAS model result.

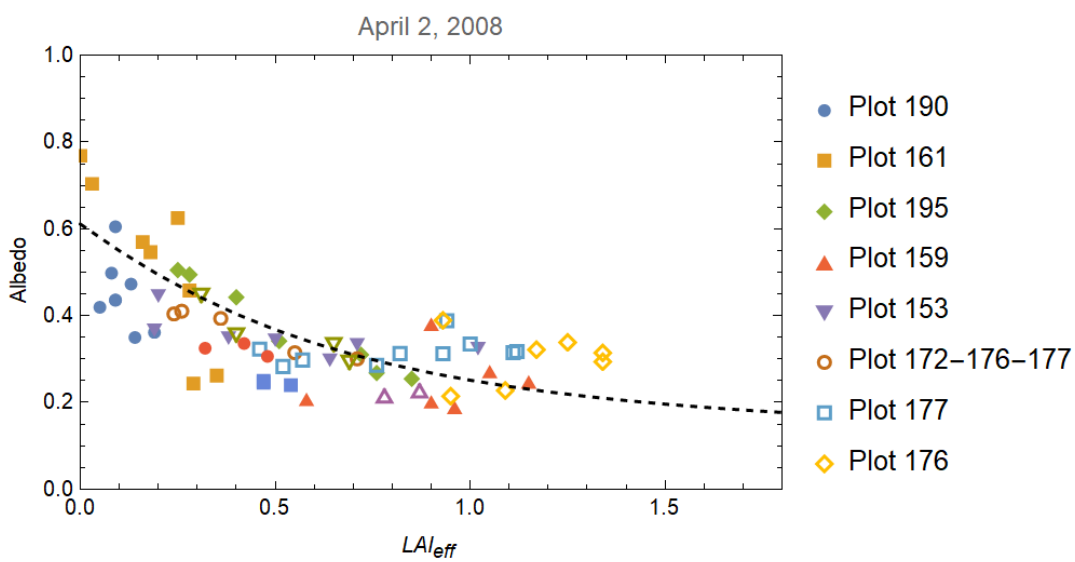

Figure 7. Variation of the airborne albedo with the airborne LAI_{eff} of the vertical profiles measured in April 2008. The vertical profile height was about 250 m. The solar zenith angle varied in the range 62.6° — 64.5° and the fraction of diffuse irradiance in the range 0.21 — 0.80. The profile height was about 200 m. The dashed curve shows the PARAS model result for the mean fraction of diffuse radiation and the mean cosine of the solar zenith angle values. The forest floor broadband albedo was taken to be the mean of albedo values measured for $LAI_{eff} = 0$.

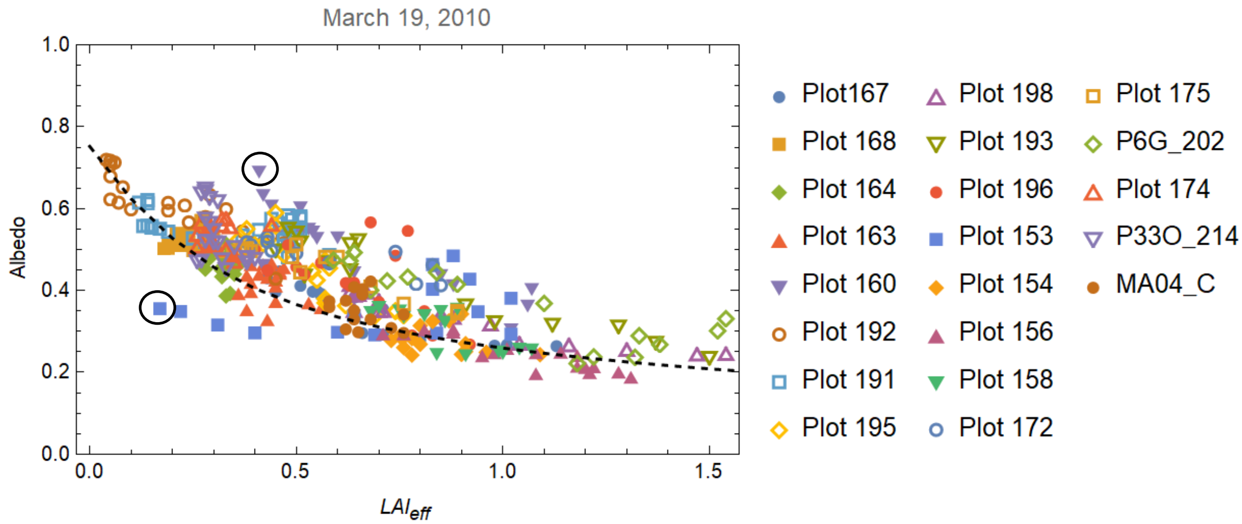

Figure 8. Variation of the airborne albedo with the airborne LAIeff of the vertical profiles measured in March 19, 2010. The solar zenith angle varied in the range 75.6° — 82.6° and the fraction of diffuse irradiance in the range 0.27 —0.63. The profile height was about 80 m. The dashed curve shows the PARAS model result for the mean fraction of diffuse radiation and the mean cosine of the solar zenith angle values. The forest floor broadband albedo was taken to be the mean of albedo values measured for $LAI_{eff} = 0$.

Figure 9. Examples of the heterogeneity effect on the albedo, circled points of Figure 8 left (Plot 160) and right (Plot 153). The left image is related to higher albedo than expected on the basis of LAI_{eff} and the right image to the opposite situation.

The relationships between the airborne albedo and LAI_{eff} was studied also for all data, not only the vertical profiles (Figure 10). All albedo values are now normalized to correspond to the solar zenith angle of 60° using the PARAS model and the single scattering albedo values derived from the model fit to the data of March 13, 2009.Then the spread of albedo values corresponding to the same LAI_{eff} was markedly larger than for the vertical profiles, because the albedo of the snow cover beneath the canopy varied as well. To some extent the large variation may also be caused by heterogeneity of the scenery, as the camera did not observe the whole area affecting the reflected radiation value. It was also evident that the level of the surface albedo decreased during the melting season so that at the end to if (April 24, 2009) the albedo was markedly lower and consequently less strongly dependent on LAI_{eff}.

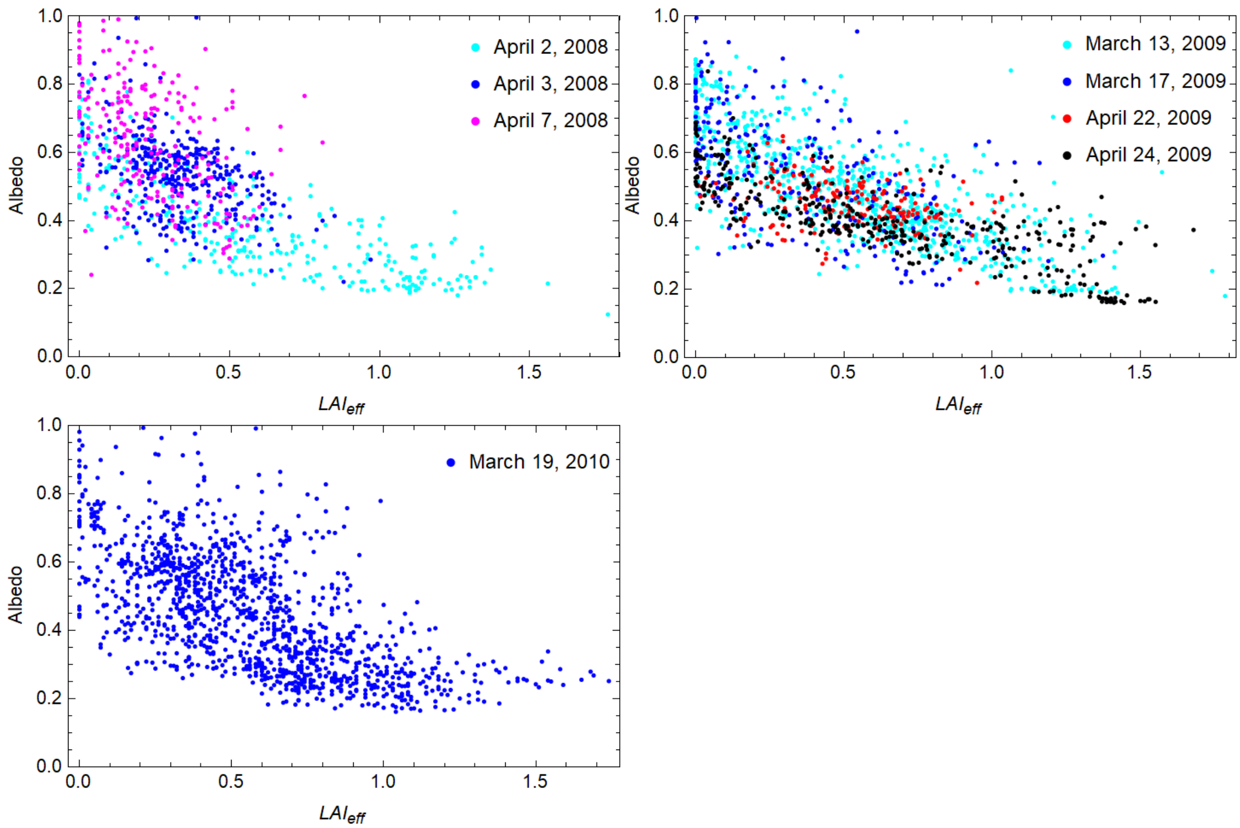

Figure 10. The airborne albedo vs. airborne LAI_{eff} for all data of flights in 2008, 2009 and 2010. The albedo has been normalized to correspond to the solar zenith angle of 60°.

The whole albedo/LAI_{eff} data set was also used to derive the relative albedo distribution, again using albedo values normalized to the solar zenith angle of 60° (Figure 11). The distributions are skewed to high values and beta distribution starting from the lowest value matches the shape well. Beta distributions parameters were derived for the whole data and data for which LAI_{eff} exceeded 0.25 and 0.5. The mean values of the distributions are given in Table 6. This manifests the effect of vegetation above snow layer on albedo. If the LAI_{eff} values smaller than 0.25 would be missing (25% of all data), the albedo would decrease from 0.49 to 0.44. Further increasing the minimum LAI_{eff} to 0.5 would drop the mean albedo to 0.4. Examples of forests with these two limit values are shown in Supplementary material (Figure S3). From the point of view of albedo, it is not only the amount of forested area that matters, but changing an open area to vegetated has a major effect. Here the effect is demonstrated with forests, but the same principle is valid for shrubs and other vegetation above the snow cover. The effect of the change in LAI_{eff} on albedo decreases with increasing LAI_{eff}.

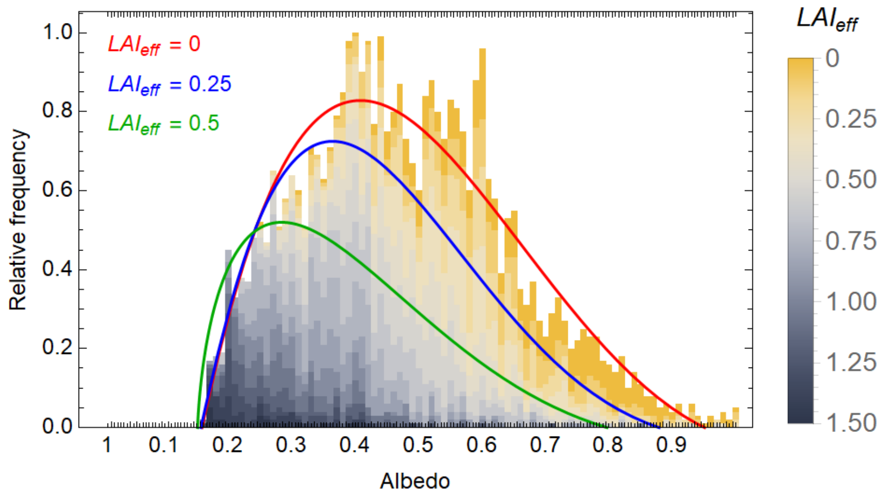

Figure 11. The relative distribution of all airborne albedo values of 2008, 2009 and 2010 normalized to the solar zenith angle value 60° and for which airborne LAI_{eff} values were available. The yellow-gray shades are related to LAI_{eff}. The area below the red, blue, and green curves consist of albedo values for which $LAI_{eff} = 0$, $LAI_{eff} = 0.25$ and $LAI_{eff} > 0.5$, respectively.

Table 6. The beta distribution parameters for the albedo and the distribution means for the whole data set and subsets with LAI_{eff} exceeding 0.25 and 0.5. The cumulative fractions of points with LAI_{eff} smaller than the minimum in question are provided too.

Minimum LAI_{eff}	Cumulative fraction of values smaller than minimum LAI_{eff}	Beta distribution parameters		Distribution mean albedo
		α	β	
0	0%	2.04	3.99	0.49
0.25	25%	2.11	5.14	0.44
0.5	53%	1.63	4.99	0.40

3.2 Variation of albedo with altitude / spatial resolution

The dynamic range of airborne albedo naturally decreased with increasing flight altitude due to the heterogeneity of the scenery. Very large uniform forested areas just don't exist in the region. On the other hand, also large open areas are rare. Already at 500 m altitude the variation range of the albedo was only about half of the range achieved at very low altitudes. The albedo would approach a constant value at about 1 km altitude. Since, the pyranometer response is dominated by an area with a radius about 10 times the measurement altitude, this would mean that a footprint of about 20 km would represent the areal average albedo. Some individual albedo values were very high, close to unity. They may be related to uneven movement of the helicopter, but it is also possible to get sun glints from large open areas with snow cover as shown before (Manninen et al., 2019).

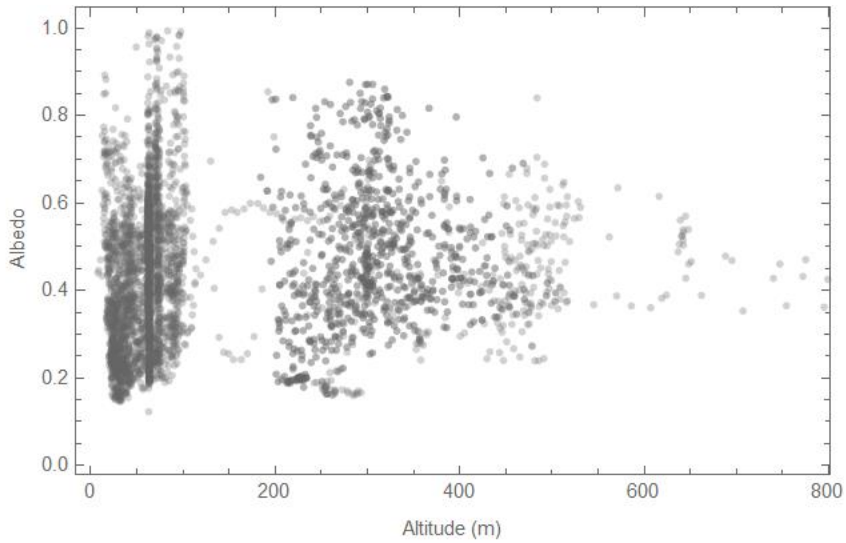

Figure 12. Albedo data from all flights vs. the flight altitude. The darkness of the point is related to the number of retrievals.

3.3 Comparison of measured albedo and satellite based albedo

The airborne albedo values were compared to the MODIS albedo product using the white-sky albedo values for the cloudy days (March 13, 2009 and April 24, 2009) and black-sky albedo values for the rest. Only the highest quality MODIS pixels were used. The reflected radiation measured by the pyranometers comes dominantly from an area with a radius 10 times the measurement altitude. Therefore, the comparison is made separately for different altitudes. The airborne albedo values were directly linked with the overlapping MODIS pixels. The results are shown in Figure 13 and Figures S4-S6 in the Supplementary material for the flights of years 2008, 2009 and 2010, respectively. For low flight altitudes the airborne measured area represented by one albedo value could be markedly smaller than that of the MODIS pixel. Even when the spatial resolution of the airborne and MODIS albedo retrievals were about similar there could be a mismatch in the albedo values due to the airborne co-ordinate being not quite at the center of the MODIS pixel. Hence, in addition to direct comparison of albedo values, also daily albedo distributions were compared (Figure 14 and Figures S7-S9 in the Supplementary material).

In general, the airborne and MODIS albedo values have good agreement, but clearly there is a wide variation range of airborne values corresponding to one MODIS pixel. In low altitude flights the airborne albedo distribution is typically wider than the MODIS albedo distribution, which is related to the larger dynamic variation of albedo in higher spatial resolution. In some cases, the distributions differ, because during those flights the airborne measurements have been focused for certain targets, so that the sampling does not cover the whole MODIS pixel. The vertical profiles were flown above forests, hence in those days the airborne distributions have more dark values (April 2, 2008; March 13, 2009 and March 19, 2010). In March 18, 2010, the focus was on bright targets, such as aapa mire and lake ice snow cover. The darker distribution of the MODIS albedo product of April 24, 2009 as compared to that of April 22, 2009 may be a result of more open water and bare soil due to the progress of melting during the 16 days from which the MODIS product is compiled. In April 24, 2009 there was not yet open water, hence the airborne albedo is brighter than that of the MODIS product.

The slightly brighter airborne distributions of May 4 and May 5, 2009 are due to their focus being on fractional snow cover, which was not a dominating feature at that time.

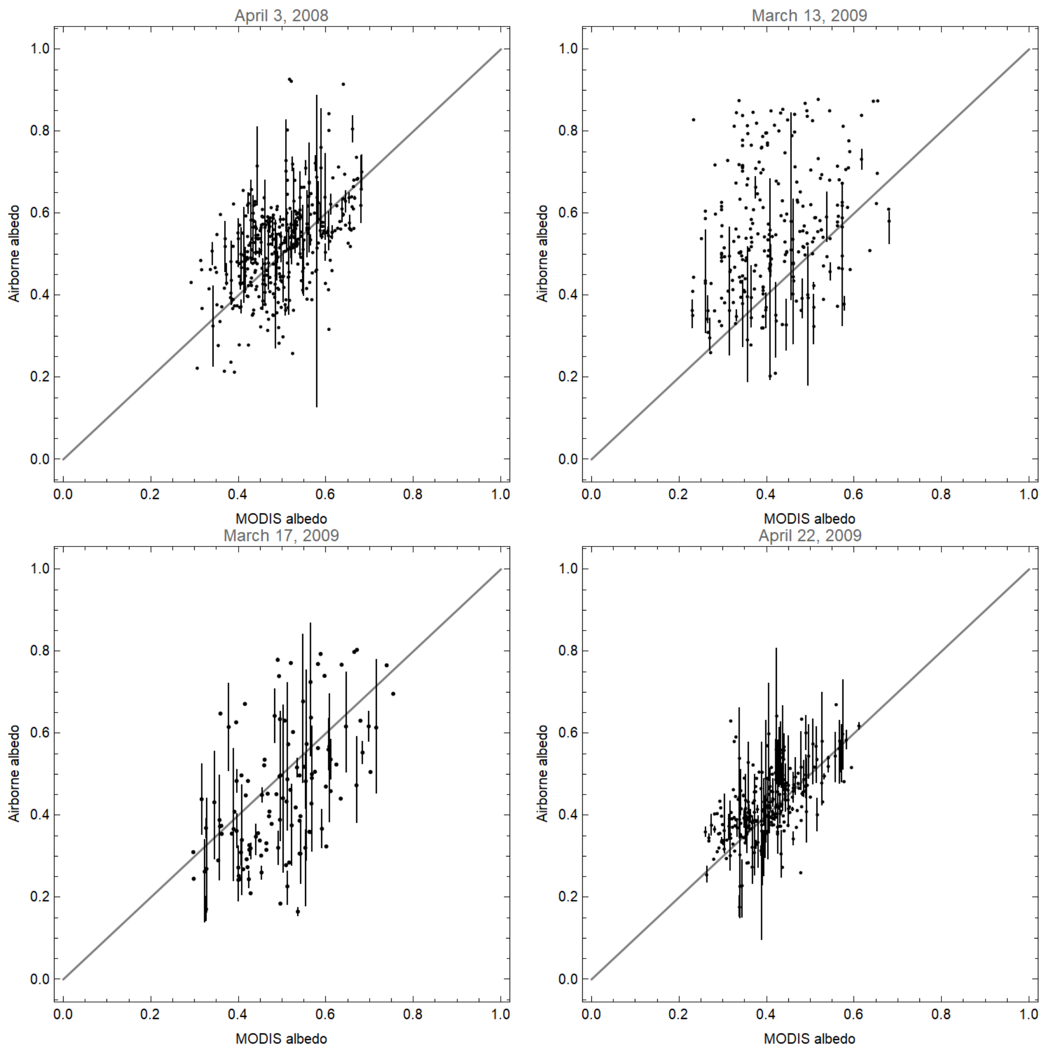

Figure 13. The airborne albedo values measured in April 3, 2008, March 13, March 17, and April 22, 2009 vs. the MODIS albedo value (MCD43A3, Albedo_WSA_shortwave for March 13 and Albedo_BSA_shortwave for the rest). The mean airborne value within a MODIS pixel is shown as a point and the variation range as a vertical line.

The large variation range of individual airborne albedo values corresponding to a MODIS pixel is to a large extent related to variation of LAI_{eff} measured from the helicopter simultaneously with the albedo (Figure 15). As the camera objective is wide optics, but not a fish-eye lens, the airborne LAI_{eff} presents the central part of the area affecting the reflected radiation value observed by the downwards looking pyranometers. If the surrounding area is completely different, then the LAI_{eff} does not correspond to the measured value well, which can be seen in individual points of Figure 15.

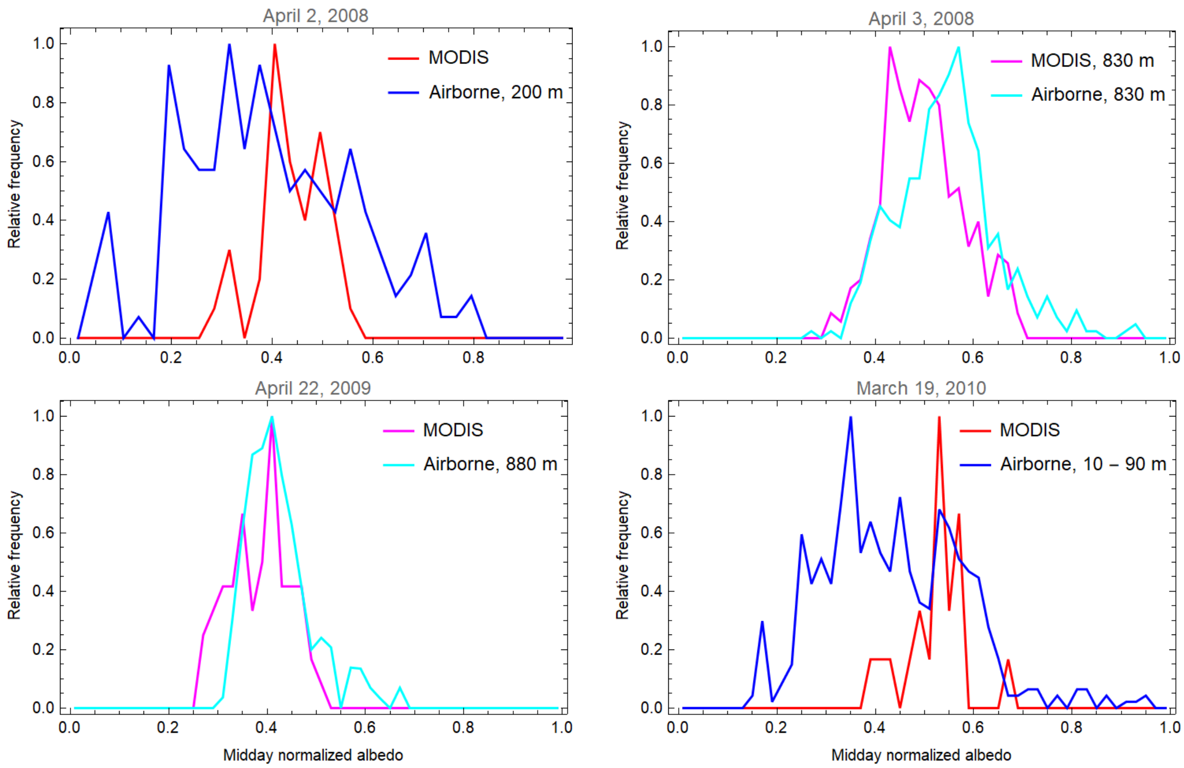

Figure 14. The relative distributions of airborne albedo values measured in April 2, 2008, April 3, 2008, April 22, 2009 and March 19, 2010 and the MODIS albedo values of corresponding pixels (MCD43A3, Albedo_BSA_shortwave).

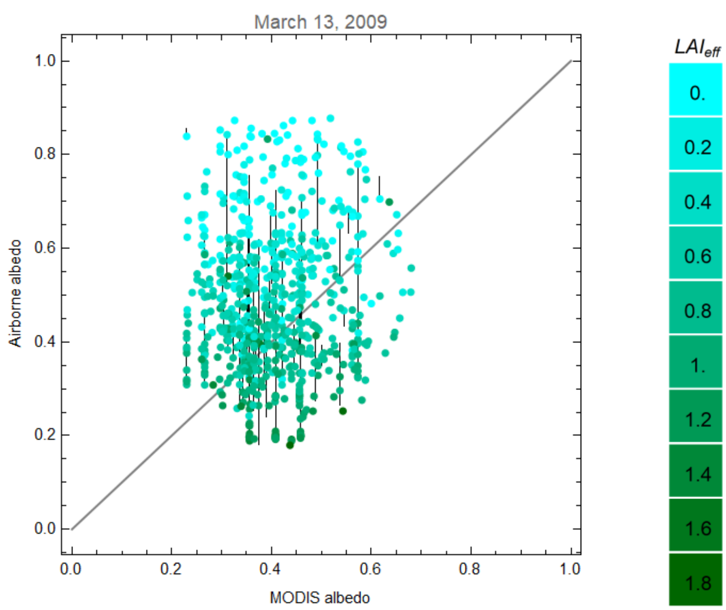

Figure 15. The airborne albedo values measured in March 13, 2009 vs. the MODIS albedo value (MCD43A3, Albedo_WSA_shortwave). The individual point color is related to the corresponding airborne measure LAI_{eff} value and the vertical line shows the variation range of the airborne albedo values within a MODIS pixel.

4 Discussion

The presence of high vegetation at snow covered areas affects the scenery albedo in different ways. Besides altering the snow microstructure and surface roughness, it casts shadows on the snow surface and increases the multiple scattering of solar radiation (Manninen & Stenberg 2009, Manninen & Jääskeläinen 2018; Jääskeläinen and Manninen, 2021). The large effect of vegetation protruding above the snow surface on surface albedo comes from the substantial spectral difference between the albedo of snow and the albedo of plant stands. Therefore, the vegetation and snow scenery albedo evolves rapidly, depending closely on both vegetation architecture and snow coverage and properties as a function of solar geometry. Small changes in either of these can potentially have a significant effect on the albedo.

With a dense vegetation canopy the snow surface is already largely covered by vegetation, and thus the increase in LAI or vegetation coverage does not significantly affect the albedo. With a sparse vegetation canopy and dominating open snow cover, increasing LAI means increasing coverage and shadowing of the snow, and through that, lower wintertime albedo. Even relatively small shrubs can have a significant effect in such case. For example, Sturm et al. (2005) found that if shrubs protrude above the snow and cover 10% of the surface, the albedo will decrease by 30%. With climate change also the treeline of subarctic forests has shown to move to higher altitudes (Sutinen et al., 2012), which will inevitably decrease the wintertime albedo of hilly terrain. Also, in other forested parts of Finland the albedo has been shown to have decreased since 1980’s by 0.02 - 0.03 per decade due to increased stem volume (Manninen et al., 2019). In the measured data of this study 25% had smaller LAI_{eff} than 0.25, thus being targets of high risk of marked albedo change.

Several studies show changes in the vegetation of the Arctic (Piao et al. 2011, Berner et al. 2020, Buitenwerf 2015). In many places the sub-Arctic plant productivity has increased. The tundra areas have witnessed a significant increase in shrub coverage and size (Forbes et al. 2010). Shrub abundance also enhances the melt in the spring causing earlier snow melt, which also decreases the albedo of the sub-Arctic and increases the absorption of solar energy to the ground. This has a potentially significant effect on the surface albedo of the sub-Arctic areas, were tundras are traditionally open areas and forest vegetation in the northern areas of the boreal forest zone is sparse. In the sub-Arctic the snow covers the ground until May, during which time there is already considerable amount of sunlight. Consequently, any changes in albedo will inevitably also affect the energy balance.

5 Conclusions

Helicopter can be used successfully to measure simultaneously airborne albedo and LAI_{eff}. The relationship of airborne albedo and LAI_{eff} does not show a marked flight altitude dependence and it agrees well with the PARAS model, which can be used for normalizing albedo to other solar zenith angle values. The airborne albedo variation range decreases essentially, when the measurement altitude increases up to 500 m and reduces at about 1 km altitude to an aerial average. The albedo of forested area with snow covered floor decreases with increasing LAI_{eff}, the change being markedly larger for smallest LAI_{eff} values. The mean albedo of the area as presented by the measurements of this study would decrease from 0.49 to 0.44, if the points with LAI_{eff} smaller than 0.25 (25% of all points) were removed.

The airborne albedo distributions agreed in general with those of the MODIS albedo product MCD43A3. The differences between pixelwise values were explained by differences in spatial resolution and representativity related to airborne measurements being focused on only certain targets, such as forest and partial snow cover.

Acknowledgments, Samples, and Data

This work was financially supported by EUMETSAT via the H-SAF visiting scientist funding and via the Climate-SAF and LSA-SAF Federate Activity funding, by European community in the Life+ project MONIMET (grant agreement LIFE12 ENV/FI000409) and by the Academy of Finland project OPTICA (295874). The work of Roujean and Hautecoeur was supported by LapBIAT.

The authors are grateful to Mr. Antti Poikonen for constructing the airborne pyranometer measurement system, Mr. Antti Aarva for instrumental calibration and black plate shielding of the pyranometers used and to Mr. Jani Poutiainen for help in the design of the measurement configuration. Co-operation with Emerita prof. Pauline Stenberg from University of Helsinki in the LAI work is gratefully acknowledged and the team is grateful to her for lending the hemispherical camera used for ground based LAI measurements. The authors wish to thank also Dr. Eero Rinne for participation in the technical test flights of the Karhukamera system used for airborne LAI retrieval. The contribution of the staff of FMI, FMI-ARC, Heliflite and Vogon-IT is gratefully acknowledged.

The data will be available in the FMI Research Data Repository: https://fmi.b2share.csc.fi/.

References

Anttila, K., Manninen, T., Jääskeläinen, E., Riihelä, A., & Lahtinen, P. (2018), The Role of Climate and Land Use in the Changes in Surface Albedo Prior to Snow Melt and the Timing of Melt Season of Seasonal Snow in Northern Land Areas of 40N–80N during 1982–2015. *Remote Sensing, 10*, 1619. doi:10.3390/rs10101619.

Anttila, K., Jääskeläinen, E., Riihelä, A., Manninen, T., Andersson, K., & Hollman, R. (2016), *Algorithm Theoretical Basis Document*: CM SAF Cloud, Albedo, Radiation Data Record Ed. 2—Surface Albedo. Available online: https://icdc.cen.uni-hamburg.de/fileadmin/user_upload/icdc_Dokumente/EUMETSAT-CMSAF/SAF_CM_FMI_ATBD_GAC_SAL_2_3.pdf (accessed on June 2, 2021).

Bergstrom, A., Gooseff, M. N., Myers, M., Doran, P. T., & Cross, J. M. (2020), The seasonal evolution of albedo across glaciers and the surrounding landscape of Taylor Valley, Antarctica , *The Cryosphere, 14*, 769–788, https://doi.org/10.5194/tc-14-769-2020.

Berner, L.T., Massey, R., Jantz, P., Forbes, B.C., Macias-Fauria, M., Myers-Smith, I., Kumpula, T., Gauthier, G., Andreu-Hayles, L., Gaglioti, B.V, Burns, P., Zetterberg, P., D'Arrigo, Ro & Goetz, S.J. (2020), Summer warming explains widespread but not uniform greening in the Arctic tundra biome. *Nature Communications, 11*, 4621. https://doi.org/10.1038/s41467-020-18479-5

Betts, A., & Ball, J., (1997), Albedo over the boreal forest. *J. Geophys. Res., 102*, 28901–28909. https://doi.org/10.1029/96JD03876.

Boers, R., Mitchell, R. M. & Krummel, P. B. (1998), Correction of aircraft pyranometer measurements for diffuse radiance and alignment errors, *J. Geophys. Res.*, 103(D13), 16,753-16,758.

Bormann, K.J., Brown, R.D., Derksen, C., &Painter, T.H. (2018), Estimating snow-cover trends from space. *Nature Clim Change 8*, 924–928. https://doi.org/10.1038/s41558-018-0318-3

Brown, R. D., & Mote, P. W. (2009). The Response of Northern Hemisphere Snow Cover to a Changing Climate, *Journal of Climate, 22*(8), 2124-2145. Retrieved May 27, 2021, from https://journals.ametsoc.org/view/journals/clim/22/8/2008jcli2665.1.xml

Buitenwerf, R., Rose, L., & Higgins, S. I. (2015). Three decades of multi-dimensional change in global leaf phenology. *Nature Climate Change*, *5*(4), 364-368.

Cao, C., Lee, X., Muhlhausen, J., Bonneau, L. and Xu, J. (2018), Measuring Landscape Albedo Using Unmanned Aerial Vehicles, *Remote sensing*, 10, 1812, 16 p. doi:10.3390/rs10111812

Carrer, D., Pinault, F., Lellouch, G., Trigo, I.F., Benhadj, I., Camacho, F., Ceamanos, X., Moparthy, S., Munoz-Sabater, J., Schüller, L., & Sánchez-Zapero, J. (2021), Surface Albedo Retrieval from 40-Years of Earth Observations through the EUMETSAT/LSA SAF and EU/C3S Programmes: The Versatile Algorithm of PYALUS. *Remote Sens.*, *13*, 372. https://doi.org/10.3390/rs13030372

Derksen, C., & Brown, R. (2012), Spring snow cover extent reductions in the 2008–2012 period exceeding climate model projections, *Geophys. Res. Lett., 39*, L19504, doi:10.1029/2012GL053387.

Essery, R. (2013), Large-scale simulations of snow albedo masking by forests. *Geophys. Res. Lett. 40*, 5521–5525. https://doi.org/10.1002/grl.51008.

Forbes, B. C., Fauria, M. M., & Zetterberg, P. (2010). Russian Arctic warming and 'greening'are closely tracked by tundra shrub willows. *Global Change Biology*, *16*(5), 1542-1554.

Gatebe, C. K., King, M. D., Platnick, S., Arnold, G. T., Vermote, E. F. & Schmid, B. (2003), Airborne spectral measurements of surface-atmosphere anisotropy for several surfaces and ecosystems over southern Africa. *J. Geophys. Res.*, 108(D13), 8489, 16 p.

Gatebe, C.K., King, M.D. Lyapustin, A.I., Arnold, G.T. & Redemann, J. (2005), Airborne Spectral Measurements of Ocean Directional Reflectance. *Journal of the Atmospheric Sciences — Special Section, 62*, 1072–1092.

GCOS (2016), The Global Observing System for Climate: Implementation Needs. Reference Number GCOS-200.

Geerts, B. & E. Linacre, 1997, The height of the tropopause. University of Wyoming. Available at http://www-das.uwyo.edu/~geerts/cwx/notes/chap01/tropo.html (Retrieved April 29, 2021).

Govaerts, Y., Lattanzio, A., Taberner, M. & Pinty, B. (2008), Generating global surface albedo products from multiple geostationary satellites. *Remote Sensing of Environment, 112*, 2804-2816. 10.1016/j.rse.2008.01.012.

Hovi A., Raitio P., & Rautiainen M. (2017), A spectral analysis of 25 boreal tree species, *Silva Fennica*, *51*(4), article id 7753. https://doi.org/10.14214/sf.7753

Jääskeläinen, E., & Manninen, T., (2021), The effect of snow at forest floor on boreal forest albedo diurnal and seasonal variation during the melting season. *Cold Regions Science and Technology*, 185, 103249, 13 p.

Kahle, A.B., (1968), Global radiation emerging from a Rayleigh-scattering atmosphere of large optical thickness. *The Astrophysical Journal*, 151, 637–645.

Karlsson, K. G., Anttila, K., Trentmann, J., Stengel, M., Fokke Meirink, J., Devasthale, A., Hanschmann, T., Kothe, S., Jääskeläinen, E., Sedlar, J., Benas, N., van Zadelhoff, G.-J., Schlundt, C., Stein, D., Finkensieper, S., Håkansson, N., & Hollmann, R. (2017), CLARA-A2: the second edition of the CM SAF cloud and radiation data record from 34 years of global AVHRR data. *Atmospheric Chemistry and Physics*, *17*(9), 5809-5828.

Levy, C.R., Burakowski, E. & Richardson, A.D. (2018), Novel Measurements of Fine-Scale Albedo: Using a Commercial Quadcopter to Measure Radiation Fluxes. *Remote Sensing*, 10, 1303, 14 p. doi:10.3390/rs10081303

Liang, S., (2000). Narrowband to broadband conversions of land surface albedo I: algorithms. *Remote Sens. Environ. 76*, 213–238. https://doi.org/10.1016/S0034-4257(00)00205-4.

Liu, Q., Wang, L., Qu, Y., Liu, N., Liu, S., Tang, H., & Liang, S. (2013), Preliminary evaluation of the long-term GLASS albedo product. *International Journal of Digital Earth, 6*, 69-95. 10.1080/17538947.2013.804601.

Lucht, W., Schaaf, C. B., & Strahler, A. H., (2000), An algorithm for the retrieval of Albedo from space using semiempirical BRDF models. *IEEE Trans. Geosci. Remote Sens., 38*, 977–998, https://doi.org/10.1109/36.841980.

Manninen, T. & Riihelä, A., (2009), ENVISAT/ASAR VV/HH backscattering and the radiation characteristics of Subarctic boreal fores., Proc. of PolInSAR 2009, 26-30 January 2009, Frascati, Italy, Special publication of ESA SP-668, 8 p.

Manninen, T. & Jääskeläinen, E., (2018), The effect of boreal forest canopy on snow covered terrain broadband albedo, *Geophysica, 53*(1), 7–27.

Manninen, T. & Roujean, J.-L. (Eds.), (2014), SNORTEX, SNOW REFLECTANCE TRANSITION EXPERIMENT, Finnish Meteorological Institute, Reports 2014:7, 68 p.

Manninen, T. & Stenberg, P. (2009), Simulation of the effect of snow covered forest floor on the total forest albedo, *Agricultural and Forest Meteorology, 149*(2), 303-319.

Manninen, T., Aalto, T., Markkanen, T., Peltoniemi, M., Böttcher, K., Metsämäki, S., Anttila, K., Pirinen, P., Leppänen, A., & Arslan, A.N., (2019), Monitoring changes in forestry and seasonal snow using surface albedo during 1982–2016 as an indicator. *Biogeosciences, 16*, 223–240. https://doi.org/10.5194/bg-16-223-2019

Manninen, T., Anttila, K., Jääskeläinen, E., Riihelä, A., Peltoniemi, J., Räisänen, P., Lahtinen, P., Siljamo, N., Thölix, L., Meinander, O., Kontu, A., Suokanerva, H., Pirazzini, R., Suomalainen, J., Hakala, T., Kaasalainen, S., Kaartinen, H., Kukko, A., Hautecoeur, O. & Roujean, J.-L. (2021), Effect of small-scale snow surface roughness on snow albedo and reflectance. *The Cryosphere*, 15, 793–820. https://doi.org/10.5194/tc-15-793-2021

Manninen, T., Jääskeläinen, E. & Riihelä, A. (2019), Black and White-Sky Albedo Values of Snow: In Situ Relationships for AVHRR-Based Estimation Using CLARA-A2 SAL, *Canadian Journal of Remote Sensing*, 18 p., DOI: 10.1080/07038992.2019.1632177

Manninen, T., Jääskeläinen, E. & Riihelä, A. (2020), Diurnal Black-Sky Surface Albedo Parameterization of Snow. *Journal of Applied Meteorology and Climatology, 59* (9): 1415–1428. DOI: https://doi.org/10.1175/JAMC-D-20-0036.1

Manninen, T., Korhonen, L., Riihelä, A., Lahtinen, P., Stenberg, P., Roujean, J.-L. & Hautecoeur, O. (2012), Boreal forest albedo and LAI in SNORTEX 2008-2010, Proc. of IGARSS'12, 978-1-4673-1159-5/12, pp. 3335 – 3338.

Manninen, T., Korhonen, L., Voipio, P., Lahtinen, P. & Stenberg, P. (2009), Leaf Area Index (LAI) Estimation of Boreal Forest Using Wide Optics Airborne Winter Photos, *Remote Sensing, 1*(4), 1380-1394.

Manninen, T., Korhonen, L., Voipio, P., Lahtinen, P. & Stenberg, P. (2012), Airborne estimation of boreal forest LAI in winter conditions: A test using summer and winter ground truth, *IEEE Transactions on Geoscience and Remote Sensing, 50*(1), 68-74. 10.1109/TGRS.2011.2173939.

Miller, J.B. (1967). A formula for average foliage density. *Australian Journal of Botany*, 15, 141-144.

Natraj, V. & Hovenier, J. W., (2012), Tables of X-, Y-, K-, and L- Functions Relevant to Rayleigh Scattering Atmospheres. Dataset] (Unpublished). https://resolver.caltech.edu/CaltechAUTHORS:20120206-140559033 (Retrieved April 29, 2021).

Nobis, M., & Hunziker, U. (2005), Automatic thresholding for hemispherical canopy-photographs based on edge detection. *Agricultural and Forest Meteorology, 128*, 243-250.

Piao, S., Wang, X., Ciais, P., Zhu, B., Wang, T. A. O., & Liu, J. I. E., (2011), Changes in satellite-derived vegetation growth trend in temperate and boreal Eurasia from 1982 to 2006. *Global Change Biology, 17*(10), 3228-3239.

Predoehl, M.C. & Spano, A.F., (1965), Airborne albedo measurements over the Ross Sea, October-Noember 1962, *Monthly Weather Review, 93*(11), 687–696.

Rautiainen, M., & Stenberg, P., (2005), Application of photon recollision probability in coniferous canopy reflectance simulations. *Remote Sensing of Environment, 96*, 98–107. doi:10.1016/j.rse.2005.02.009.

Ridler, T.W., & Calvard, S., (1978), Picture thresholding using an iterative selection method. *IEEE Transactions on Systems, Man and Cybernetic,s 8*: 630-632.

Riihelä, A., Laine, V., Manninen, T., Palo, T., & Vihma, T. (2010), Validation of the Climate-SAF surface broadband albedo product: Comparisons with in situ observations over Greenland

and the ice-covered Arctic Ocean. *Remote Sensing of Environment, 114*(11), 2779–2790. https://doi.org/10.1016/J.RSE.2010.06.014

Román, M.O., Gatebe, C.K., Shuai, Y., Wang, Z., Gao, F., Masek, J.G., He, T., Liang, S., & Schaaf, C.B., (2013), Use of In Situ and Airborne Multiangle Data to Assess MODIS- and Landsat-Based Estimates of Directional Reflectance and Albedo. *IEEE Transactions on Geoscience and Remote Sensing, 51*(3), 1393-1404.

Román, M.O., Gatebe, Schaaf, C.B., Poudyal, R., Wang, Z. & King, M.D., (2011), Variability in surface BRDF at different spatial scales (30 m–500 m) over a mixed agricultural landscape as retrieved from airborne and satellite spectral measurements. *Remote Sensing of Environment, 115*, 2184–2203.

Ryan, J.C., Hubbard, A., Box, J.E., Brough, S., Cameron, K., Cook, J.M., Cooper, M., Doyle, S.H., Edwards, A., Holt, T., Irvine-Fynn, T., Jones, C., Pitcher, L.H., Rennermalm, A.K., Smith, L.C., Stibal, M. & Snooke, N. (2017), Derivation of High Spatial Resolution Albedo from UAV Digital Imagery: Application over the Greenland Ice Sheet. *Front. Earth Sci., 5*(40), 13 p. doi: 10.3389/feart.2017.00040

Schaaf, C. B., Gao, F., Strahler, A. H., Lucht, W., Li, X., Tsang, T., Strugnell, N.C., Zhang, X., Jin, Y., Muller, J.-P., Lewis, P., Barnsley, M, Hobson, P., Disney, M., Roberts, G., Dunderdale, M., Doll, C., d'Entremont, R.P., Hu, B., Liang, S., Privette, J.L., & Roy, D. (2002), First operational BRDF, albedo nadir reflectance products from MODIS. *Remote sensing of Environment*, *83*(1-2), 135-148.

Sekera, Z., & Kahle, A. B., (1966), Scattering Functions for Rayleigh Atmospheres of Arbitrary Thickness, Rep. R-452-PR (Santa Monica: The Rand Corporation).

Smolander, S., & Stenberg, P., (2005), Simple parameterizations of the radiation budget of uniform broadleaved and coniferous canopies. *Remote Sensing of Environment*, *94*, 355–363. doi:10.1016/j.rse.2004.10.010.

Solantie, R., (1988), Albedo in Finland on the basis of observations on aircraft, Meteorological publications No. 12, Finnish Meteorological Institute, 106 p.

Stenberg, P., (2007), Simple analytical formula for calculating average photon recollision probability in vegetation canopies. *Remote Sensing of Environment*, *109*, 221–224. doi:10.1016/j.rse.2006.12.014

Stenberg, P., Mõttus, M., & Rautiainen, M., (2016), Photon recollision probability in modelling the radiation regime of canopies — A review. *Remote Sensing of Environmentg*, *183*, 98–108. doi:doi.org/10.1016/j.rse.2016.05.013.

Stenberg, P., Nilson, T., Smolander, H., & Voipio, P., (2003), Gap fraction based estimation of LAI in Scots pine stands subjected to experimental removal of branches and stems. *Canadian Journal of Remote Sensing*, *29*, 363–370.

Sturm, M., Douglas, T., Racine, C., & Liston, G. E. (2005), Changing snow and shrub conditions affect albedo with global implications. *Journal of Geophysical Research: Biogeosciences*, *110*(G1).

Sutinen, R., Närhi, P., Middleton, M., Hänninen, P., Timonen, M., & Sutinen, M.-L., (2012), Advance of Norway spruce (Picea abies) onto mafic Lommoltunturi fell in Finnish Lapland during the last 200 years, *Boreas*, *41*, 367–378. 10.1111/j.1502-3885.2011.00238.x. ISSN 0300-9483.

Verseghy, D., McFarlane, N., & Lazare, M., (1993), CLASS - a Canadian land surface scheme for GCMs. II: vegetation model and coupled runs. *Int. J. Climatol.*, *13*, 347–370. https://doi.org/10.1002/joc.3370130402.

Webb, A.R. Stromberg, I. M., Li, H. & Bartlett, L. M., (2000), Airborne spectral measurements of surface reflectivity at ultraviolet and visible wavelengths. *Journal of Geophysical Research*, 105(D49, 4945-4948.

Webb, A.R., Kylling, A., Wendisch, M. & Jäkel, E., (2004), Airborne measurements of ground and cloud spectral albedos under low aerosol loads. *Journal of Geophysical Research*, *109*(D20205), 9 p. doi:10.1029/2004JD004768

Webster, C. & Jonas, T., (2018), Influence of canopy shading and snow coverage on effective albedo in a snow-dominated evergreen needleleaf forest. *Remote Sens. Environ.*, *214*, 48–58. https://doi.org/10.1016/j.rse.2018.05.023.

Wendisch, M., Pilewskie, P., Jäkel, E., Schmidt, S., Pommier, J., Howard, S., Jonsson, H.H., Guan, H., Schröder, M. & Mayer, B., (2004), Airborne measurements of areal spectral surface albedo over different sea and land surfaces. *Journal of Geophysical Research*, *109*(D08203), 15 p. doi:10.1029/2003JD004392

Yang, F., Mitchell, K., Hou, Y., Dai, Y., Zeng, X., Wang, Z., & Liang, X., (2008), Dependence of land surface albedo on solar zenith angle: observations and model parameterization. *J. Appl. Meteorol. Climatol.*, *47*, 2963–2982. https://doi.org/10.1175/2008JAMC1843.1.

Appendix A: The flight routes during the SNORTEX campaign

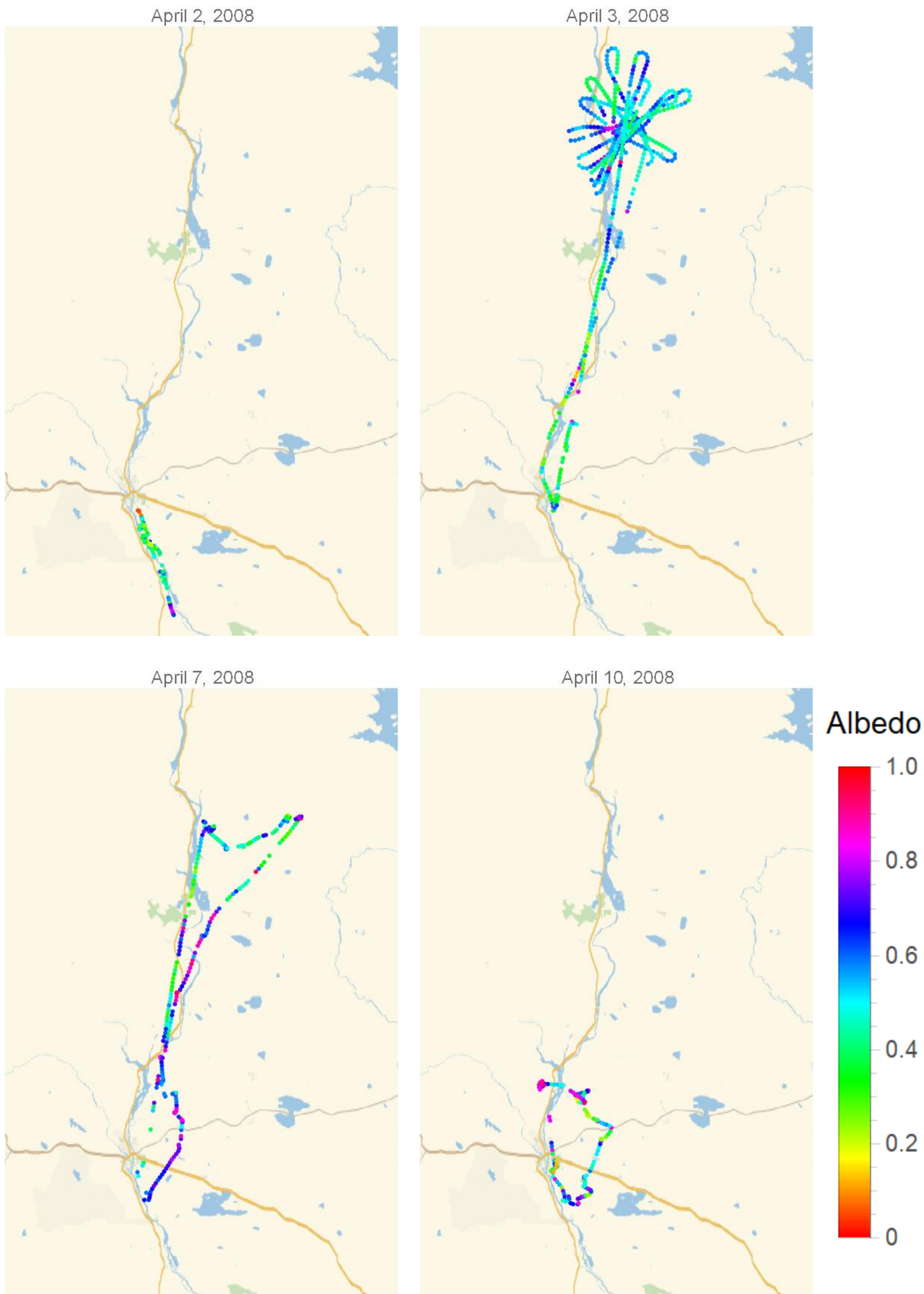

Figure A1. The flight routes of April 2, April 3, April 7, and April 10 in 2008. The lower left and upper right corner co-ordinates are (67.25°N, 26.22°E) and (67.95°N, 27.39°E), respectively. The crossroads of Sodankylä center are near the starting point of all flights. The background map is provided by Wolfram Research.

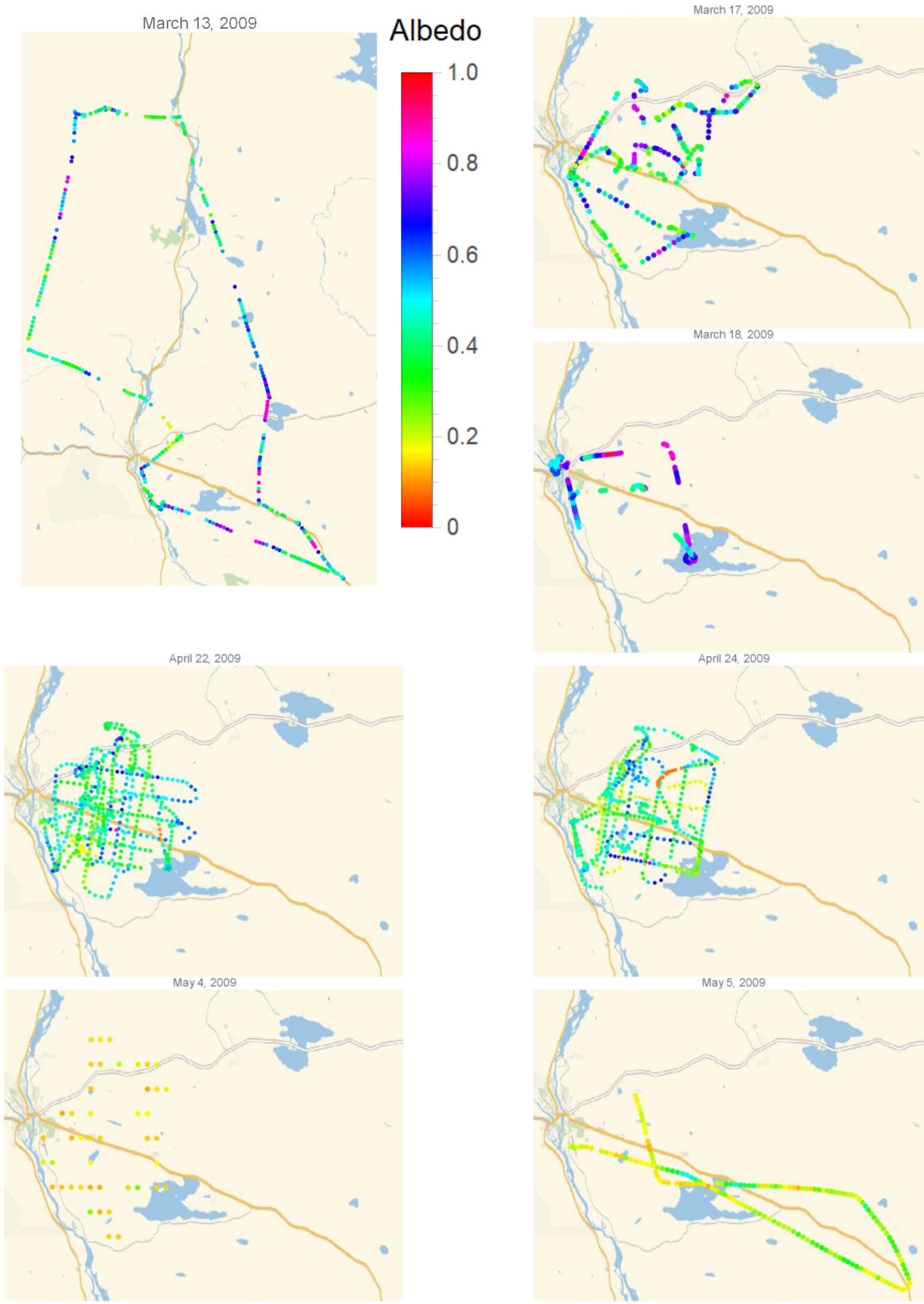

Figure A2. The flight routes of March 13, March 17, March 18, April 22, April 24, May 4, and May 5 in 2009. The lower left and upper right corner co-ordinates are (67.25°N, 26.22°E) and (67.95°N, 27.39°E) for March 13; and (67.29°N, 26.55°E) and (67.5°N, 27.25°E) for the rest. The background map is provided by Wolfram Research.

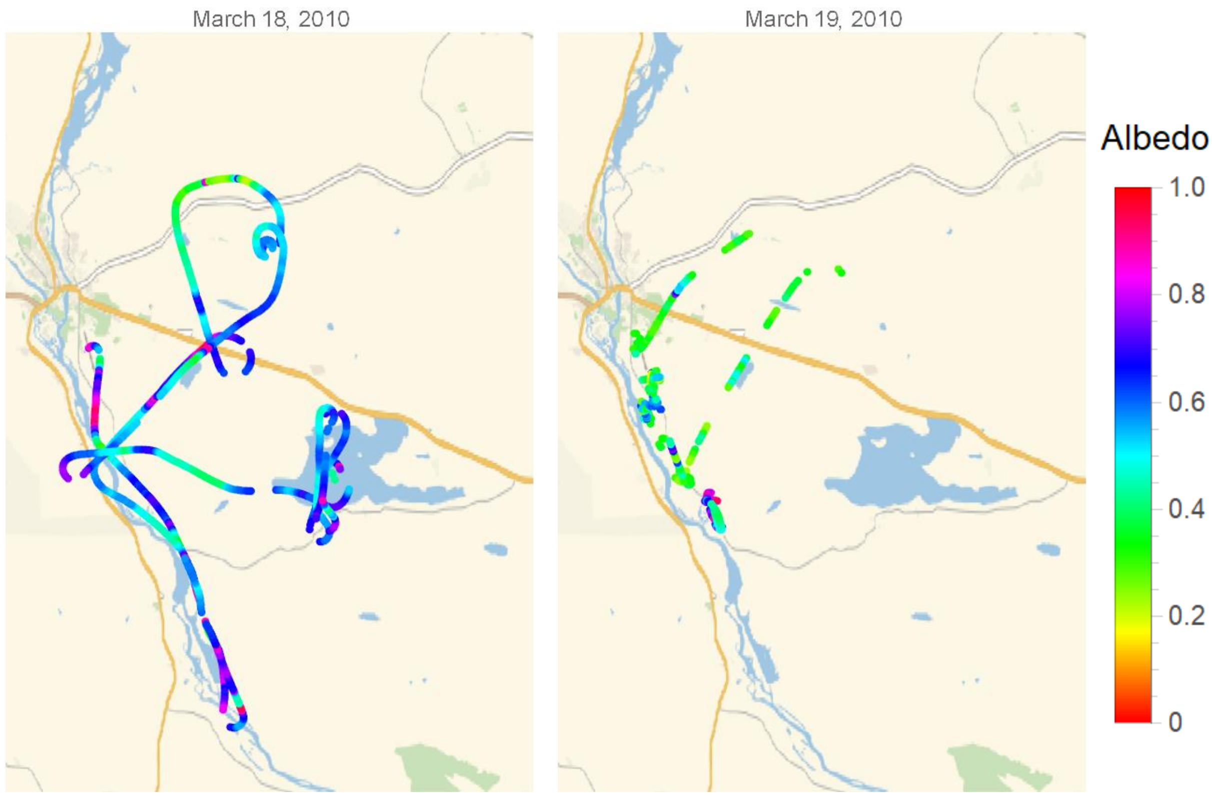

Figure A3. The flight routes of April 2, April 3, April 7, and April 10 in 2008. The size of the point is related to the albedo value. The lower left and upper right corner co-ordinates are (67.25°N, 26.55°E) and (67.5°N, 27.0°E). The background map is provided by Wolfram Research.

Appendix B: Comparison of left and right pyranometer observations

Table B1. The coefficient of determination for linear relationships between the left and right global and reflected radiation measured from the helicopter for all data. Notice that the R^2 values were derived for a linear regression without allowing an offset.

Date	Sky conditions during the azimuthal calibration	R^2	
		Airborne Global Right vs. left	Airborne Reflected Right vs. left
April 2, 2008	Clear	0.013	0.976
April 3, 2008	Clear	0.152	0.978
April 7, 2008	Clear	0.496	0.979
April110, 2008	Clear	0.268	0.986
March 13, 2009	Cloudy	0.944	0.989
March 17, 2009	Perfectly clear	0.278	0.980
March 18, 2009	Clear/cloudy	0.258	0.729
April 22, 2009	Perfectly clear	0.402	0.989
April 24, 2009	Clear -> cloudy	0.004	0.990
May 4, 2009	Clear -> cloudy	0.006	0.995
May 5, 2009	Cloudy -> clear	0.148	0.994
March 18, 2010	Clear/cloudy	0.200	0.984
March 19, 2010	Clear/cloudy	0.005	0.798

Appendix C: Albedo model formulas of the PARAS model

In the extended PARAS albedo model (Manninen and Stenberg, 2009), the black-sky spectral forest albedo (α_{black}) is a sum of four components:

$$\alpha_{black} = \alpha_{tt} + \alpha_s + \alpha_{st} + \alpha_{ss} \tag{C1}$$

where α_{tt} is the pure forest floor scattering part, α_s is the pure canopy scattering, α_{st}denotes the multiple scattering between forest floor and canopy with the last hit from the floor, and α_{ss} is the multiple scattering between forest floor and canopy with the last hit from the canopy. To achieve more compact version of the α_{black}, the multiple scattering components α_{st} and $\alpha_{ss}$are reformulated:

$$\alpha_{black} = \alpha_{tt} + \alpha_s + \alpha'_{st} + \alpha'_{ss} \tag{C2}$$

where

$$\alpha_{tt} = k\alpha_b t_0^2 + (1-k)\alpha_b t_0 t_1 \tag{C3}$$

$$\alpha_s = Q(1-t_0) \cdot \frac{\omega_L - p\omega_L}{1-p\omega_L} \tag{C4}$$

$$\alpha'_{st} = \{\alpha_b(1-Q_b)[kt_0(1-t_0) + (1-k)t_0(1-t_1)]\} \cdot \frac{\omega_L - p\omega_L}{1-p\omega_L} \tag{C5}$$

$$\alpha'_{ss} = \Big\{\alpha_b\big[(1-Q)(1-t_0) + Q_b\alpha_b t_0\big(k(1-t_0) + (1-k)(1-t_1)\big)\big] \cdot \frac{t_1(1-\omega_L + Q_b\omega_L - Q_b p\omega_L) + (1-Q_b)(\omega_L - p\omega_L)}{1 - p\omega_L - Q_b\alpha_b(1-t_1)(\omega_L - p\omega_L)}\Big\} \cdot \frac{\omega_L - p\omega_L}{1-p\omega_L} \tag{C6}$$

Now α'_{st} consists of the portion of multiple scattering where radiation escapes upwards from canopy scattering after being first scattered from the forest floor, and α'_{ss}contains the rest of the multiple scattering (including radiation scattering several times between canopy and forest floor).

The uncollided canopy transmittance in direct (t_0) and diffuse (t_1) radiation conditions are:

$$t_0 = exp\left(-\frac{G \cdot LAI_{eff}}{\cos(\theta)}\right) \tag{C7}$$

and

$$t_1 = exp\big(-G \cdot LAI_{eff}\big)\big(1 - G \cdot LAI_{eff}\big) - \big(G \cdot LAI_{eff}\big)^2 Ei\big(-G \cdot LAI_{eff}\big) \tag{C8}$$

where θ is the solar zenith angle, G is the radiation extinction coefficient of a uniform leaf canopy, LAI_{eff} is the effective leaf area index, and Ei is the exponential integral.

The formula for photon recollision probability p is from Stenberg (2007):

$$\hat{p} = 1 - \frac{1-t_1}{LAI_{eff}/\beta} \quad \text{(C9)}$$

where β is the clumping index, which equals unity for broadleaved canopy and is smaller than unity for coniferous canopy. For broadleaved forests $\beta = 1$ and for coniferous forests $\beta = 0.67$ (Stenberg et al., 2003). The leaf single scattering albedo ω_L, the forest floor albedo α_b, the fraction of incoming radiation scattered upwards by the canopy Q, and the portion of radiation reflected by the forest floor and then scattered downwards by the canopy Q_b are all wavelength dependent parameters. Forest floor albedo is a combination of a purely Lambertian surface and a completely forward/backward scattering surface. A parameter k is used to indicate the weight of the forward/backward scattering part.

The white-sky spectral forest albedo (α_{white}) is modeled similarly as the black-sky albedo. Only difference is that the calculations are done by integrating over solar zenith angle. The four component sum is:

$$\alpha_{white} = \alpha_{difftt} + \alpha_{diffs} + \alpha'_{diffst} + \alpha'_{diffss} \quad \text{(C10)}$$

where

$$\alpha_{difftt} = k\alpha_b t_2 + (1-k)\alpha_b t_1^2 \quad \text{(C11)}$$

$$\alpha_{diffs} = Q(1-t_1) \cdot \frac{\omega_L - p\omega_L}{1-p\omega_L} \quad \text{(C12)}$$

$$\alpha'_{diffst} = \{\alpha_b(1-Q_b)[k(t_1-t_2) + (1-k)t_1(1-t_1)]\} \cdot \frac{\omega_L - p\omega_L}{1-p\omega_L} \quad \text{(C13)}$$

and

$$\alpha'_{diffss} = \left\{\alpha_b\left[(1-Q)(1-t_1) + Q_b\alpha_b\left(k(t_1-t_2) + (1-k)t_1(1-t_1)\right)\right] \cdot \frac{t_1(1-\omega_L + Q_b\omega_L - Q_b p\omega_L) + (1-Q_b)(\omega_L - p\omega_L)}{1 - p\omega_L - Q_b\alpha_b(1-t_1)(\omega_L - p\omega_L)}\right\} \cdot \frac{\omega_L - p\omega_L}{1-p\omega_L} \quad \text{(C14)}$$

and where

$$t_2 = exp\left(-2G \cdot LAI_{eff}\right) \cdot \left(1 - 2G \cdot LAI_{eff}\right) - \left(2G \cdot LAI_{eff}\right)^2 Ei\left(-2G \cdot LAI_{eff}\right) \quad \text{(C15)}$$

In this study we used spherical $G = 0.5$ (assuming spherical leaf orientation distribution), and the forest floor surface was assumed to cause only diffuse scattering ($k = 1$), since the solar zenith angle was so small. It was also assumed that the scattering does not depend on the direction from which the photon enters the canopy, i.e. $Q = Q_b$, since the shape of the canopy is not described.